frontiers in Earth Science

ORIGINAL RESEARCH
published: 04 December 2018
doi: 10.3389/feart.2018.00215

Geochemistry of Noble Gases and CO_2 in Fluid Inclusions From Lithospheric Mantle Beneath Wilcza Góra (Lower Silesia, Southwest Poland)

Andrea Luca Rizzo[1,2], Beatrice Pelorosso[2], Massimo Coltorti[2], Theodoros Ntaflos[3], Costanza Bonadiman[2], Magdalena Matusiak-Małek[4], Francesco Italiano[1] and Giovanni Bergonzoni[2]*

[1] Sezione di Palermo, Istituto Nazionale di Geofisica e Vulcanologia, Palermo, Italy, [2] Dipartimento di Fisica e Scienze della Terra, Università degli Studi di Ferrara, Ferrara, Italy, [3] Department of Lithospheric Research, University of Vienna, Vienna, Austria, [4] Institute of Geological Sciences, University of Wrocław, Wrocław, Poland

OPEN ACCESS

Edited by:
Alessandro Aiuppa, Università degli Studi di Palermo, Italy

Reviewed by:
Orlando Vaselli, Università degli Studi di Firenze, Italy
Franco Tassi, Università degli Studi di Firenze, Italy
Veronique Gardien, Claude Bernard University Lyon 1, France

***Correspondence:**
Andrea Luca Rizzo
andrea.rizzo@ingv.it;
rzznrl@unife.it

Specialty section:
This article was submitted to Petrology, a section of the journal Frontiers in Earth Science

Received: *15 May 2018*
Accepted: *07 November 2018*
Published: *04 December 2018*

Citation:
Rizzo AL, Pelorosso B, Coltorti M, Ntaflos T, Bonadiman C, Matusiak-Małek M, Italiano F and Bergonzoni G (2018) Geochemistry of Noble Gases and CO_2 in Fluid Inclusions From Lithospheric Mantle Beneath Wilcza Góra (Lower Silesia, Southwest Poland). Front. Earth Sci. 6:215. doi: 10.3389/feart.2018.00215

Knowledge of the products originating from the subcontinental lithospheric mantle (SCLM) is crucial for constraining the geochemical features and evolution of the mantle. This study investigated the chemistry and isotope composition (noble gases and CO_2) of fluid inclusions (FI) from selected mantle xenoliths originating from Wilcza Góra (Lower Silesia, southwest Poland), with the aim of integrating their petrography and mineral chemistry. Mantle xenoliths are mostly harzburgites and sometimes bear amphiboles, and are brought to the surface by intraplate alkaline basalts that erupted outside the north-easternmost part of the Eger (Ohře) Rift in Lower Silesia. Olivine (Ol) is classified into two groups based on its forsterite content: (1) $Fo_{88.9-91.5}$, which accounts for a fertile-to-residual mantle, and (2) $Fo_{85.5-88.1}$, which indicates large interactions with circulating (basic) melts. This dichotomy is also related to orthopyroxene (Opx) and clinopyroxene (Cpx), which show two ranges of Mg# values (87–90 and 91–93, respectively) and clear evidence of recrystallization. CO_2 predominates within FI, followed by N_2. The $\delta^{13}C$ of mantle CO_2 varies between −4.7‰ and −3.1‰, which mostly spans the MORB range ($-8‰ < \delta^{13}C < -4‰$). The $^3He/^4He$ ratio is 6.7–6.9 Ra in Cpx, 6.3–6.8 Ra in Opx, and 5.9–6.2 Ra in Ol. These values are within the range proposed for European SCLM (6.3±0.3 Ra). The decrease in $^3He/^4He$ from Cpx to Ol is decoupled from the He concentration, and excludes any diffusive fractionation from FI. The chemistry of FI entrapped in Ol indicates that the mantle is depleted by variable extents of partial melting, while that of Opx and Cpx suggests the overprinting of at least one metasomatic event. According to Matusiak-Małek et al. (2017), Cpx, Opx, and amphiboles were added to the original harzburgite by carbonated hydrous silicate melt related to Cenozoic volcanism. This process resulted in entrapment of CO_2-rich inclusions whose chemical and isotope composition resembles that of metasomatizing fluids. We argue that FI data reflect a mixing between two endmembers: (1) the residual mantle, resulting from partial melting of European SCLM, and (2) the metasomatic agent, which is strongly He-depleted and characterized by MORB-like features.

Keywords: noble gases, CO_2, fluid inclusions, mantle xenoliths, European mantle, SCLM, MORB, metasomatism

INTRODUCTION

During the last 60–70 Myr, Europe, and the circum-Mediterranean area have experienced extensive volcanic activity related to their complex geodynamic evolution. The erupted rocks have geochemical characteristics resembling two types of magmatism: (1) orogenic with calc-alkaline magmas, generated in subduction-related settings, and (2) anorogenic with alkaline magmas, generated in intraplate conditions (Lustrino and Wilson, 2007 and references therein). Most cases of anorogenic magmatism started up to 30 Myr later than orogenic magmatism, and brought mantle-derived ultramafic xenoliths to the surface. These xenoliths represent an essential source of information about (1) the nature and evolution of the European lithospheric mantle, (2) the genesis of basic magmas, and (3) magma–mantle geochemical interactions at mantle depth or at the Earth's surface (Downes et al., 2001; Gautheron and Moreira, 2002; Coltorti et al., 2009, 2010; Bonadiman and Coltorti, 2011; Day et al., 2015).

The easternmost major exposure of Cenozoic volcanic activity in Central Europe occurs in the Eger (Ohře) Rift (Bohemian Massif) and its surroundings. The northeastern prolongation of this rift is located in Lower Silesia (southwest Poland) at the margin of the Variscan orogenic belt, where some SiO_2-undersaturated basalts carry mantle xenoliths (Ćwiek et al., 2018 and references therein). Most of these xenoliths are anhydrous spinel-bearing harzburgites and dunites, but there are also some lherzolites. Studies of these xenoliths have shown that the subcontinental lithospheric mantle (SCLM) in this area is strongly depleted (up to 35%), and has been further affected by reactions with CO_2-bearing alkaline silicate metasomatic melt, possibly related to Cenozoic volcanism (e.g., Matusiak-Małek et al., 2014, 2017 and references therein). The amount of percolating metasomatic melt would decrease continuously during this reaction, thereby progressively modifying its chemical composition. Those two factors resulted in the formation of strong heterogeneities that are visible in the modal and chemical compositions of the mantle.

A considerable amount of information about features of the mantle beneath the north-easternmost part of the Eger (Ohře) Rift can be obtained by studying the geochemistry of fluid inclusions (FI) in ultramafic xenoliths. Several studies have already demonstrated that noble gases (He, Ne, and Ar) and CO_2 systematics in FI represent an useful tool for understanding the main processes that modify the original features of the mantle both temporally and spatially (Deines, 2002; Gautheron and Moreira, 2002; Gautheron et al., 2005; Martelli et al., 2011, 2014; Correale et al., 2012, 2016; Day et al., 2015; Gennaro et al., 2017). However, contemporaneous measurements of He, Ne, and Ar isotopes in European mantle xenoliths are limited to a few sample suites. Moreover, noble gases and C isotopes of CO_2 together have never been studied in mantle xenoliths from Europe and the circum-Mediterranean area, and hence the features of the mantle and its geodynamic implications remain unclear.

To the best of our knowledge, studies of noble gases from central European mantle xenoliths have only involved the volcanic provinces of the French Massif Central, Eifel, and Pannonian Basin (Dunai and Baur, 1995; Buikin et al., 2005; Gautheron et al., 2005). These studies suggest that the $^3He/^4He$ ratio normalized to the atmosphere is 6.32 ± 0.39 Ra (mean ± SD). This range of values is lower than that MORB mantle (8±1 Ra; Graham, 2002) or plume-related settings (e.g., up to 40 Ra in Hawaii and Iceland; Stuart et al., 2003), and the origin of this radiogenic isotope signature is still debated. It has been attributed to a mantle plume with a low $^3He/^4He$ ratio due to either the addition and recycling of crustal materials to a MORB-like source (Dunai and Baur, 1995), or being an original feature of the European SCLM (Gautheron et al., 2005). On the other hand, Ne and Ar isotopes from selected suites of ultramafic xenoliths from the Eifel and Pannonian Basin have been interpreted based on the presence of a mantle plume beneath these areas (Buikin et al., 2005). However, those authors used a multistep crushing method to extract gases from mineral-hosted FI, and this approach is notably less conservative than the single-step crushing applied by Gautheron et al. (2005) because it can result in the release of radiogenic and cosmogenic noble gases trapped within the crystal lattice. The consequences of this methodological difference need to be carefully evaluated and compared.

The present study is the first to investigate the chemistry and isotope composition of noble gases and CO_2 hosted in FI from mantle xenoliths found in basanite rocks from Wilcza Góra (WG) in Lower Silesia, southwest Poland. These data were integrated with the main information obtained in mineralogical and petrological studies to define the features of the mantle beneath this sector of the European SCLM and interpret the results in the context of other European mantle xenoliths. We also compare the isotope composition of FI with that of surface gases emitted along the Eger (Ohře) Rift.

GEODYNAMIC AND GEOLOGICAL SETTING

Anorogenic, mostly mafic volcanism has occurred in Central Europe (in the French Massif Central, Rhenish Massif, and Bohemian Massif) from the Cenozoic to the Pleistocene to form the Cenozoic central European Volcanic Province (Wilson and Downes, 2006; Lustrino and Wilson, 2007; CEVP). This volcanism occurred during the convergence between the African and European plates along with the progressive closure of oceanic basins in the Mediterranean region and the formation of the Alpine orogeny. Within this compressional regime, an extensional phase triggered the opening of the European Cenozoic Rift System (ECRS) (Dèzes et al., 2004), whose products occur typically in the proximity of graben systems. The north-easternmost part of the CEVP is related to the northeast–southwest trending Eger (Ohře) Rift in the western part of the Bohemian Massif in the Czech Republic (**Figure 1A**). Volcanic rocks occur both along the rift axis and in the off-rift environment in this area (Ulrych et al., 2011). Volcanic rocks located northeast of the rift in southwest Poland follow the northwest–southeast trending Odra fault zone (**Figure 1A**). Volcanism in southwest Poland has exhibited three main activity peaks: (1) Eocene-Oligocene (34–26 Ma), (2) Miocene

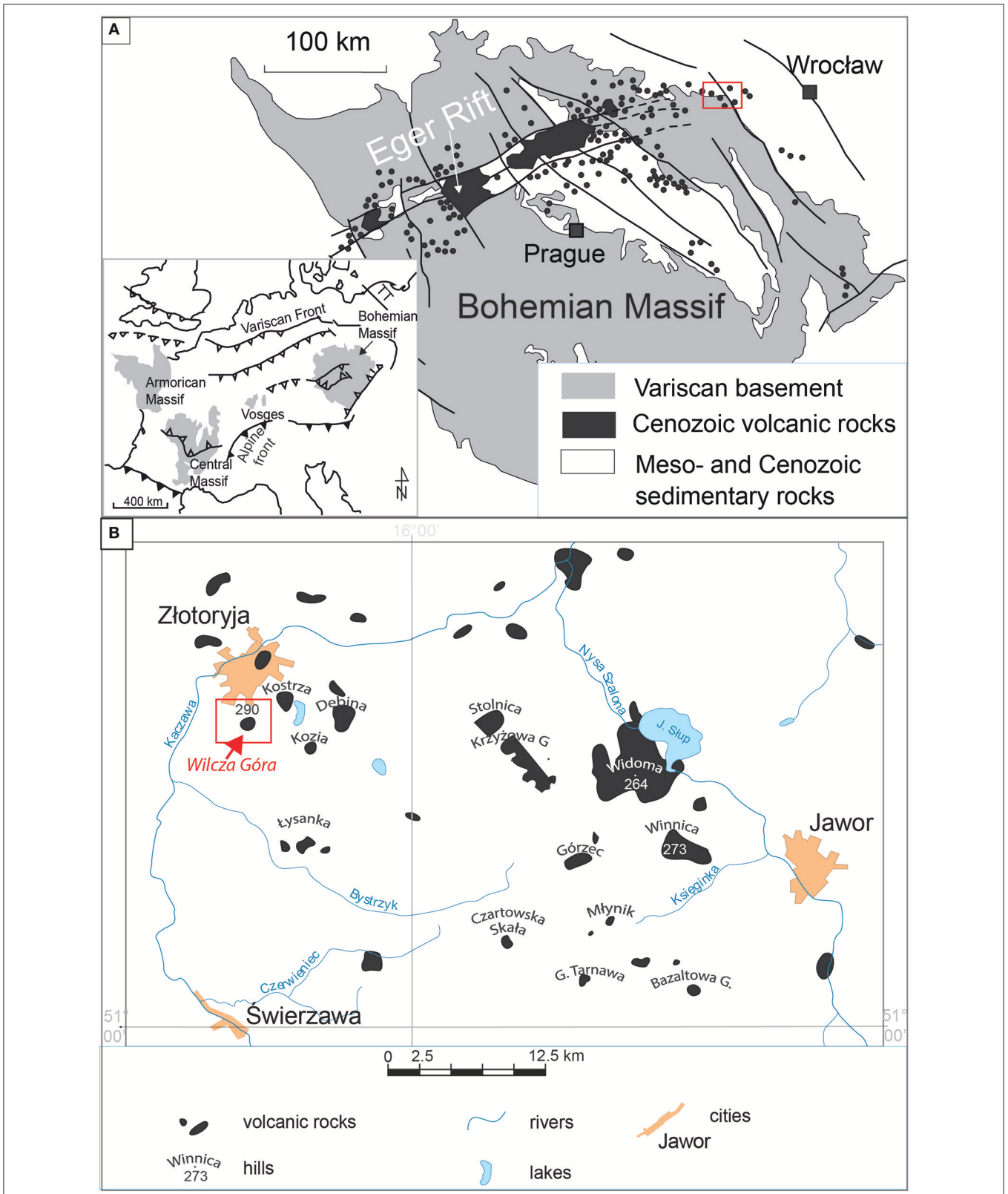

FIGURE 1 | (A) Location of Eger Rift in Bohemian Massif (based on Ulrych et al., 2011), inset shows European Variscan Basement and major fault zones (Mazur et al., 2006, modified); **(B)** Outcrops of Cenozoic volcanic rocks in the vicinity of Złotoryja city, location of Wilcza Góra indicated by arrow and red box (based on Sawicki, 1995).

(22–18 Ma), and (3) Pliocene-Pleistocene (5.5–1.0 Ma) (Pécskay and Birkenmajer, 2013). More than 300 outcrops of Cenozoic mafic volcanic rocks have been identified in southwest Poland, and around 3% of them contain xenoliths originating from the upper mantle and lower crust (Matusiak-Małek et al., 2017).

The present study investigated mantle xenoliths from WG basanite rocks (20.07 ± 0.90 Ma) (Birkenmajer et al., 2007) located in the Kaczawskie Mountains around 40 km east of the axis of the Eger Graben. These mountains constitute the western part of the Sudetes mountain range, which constitutes the northern part of the Bohemian Massif and was amalgamated during the Variscan closure of the Rheic Ocean ca. 370 Ma (Mazur et al., 2006 and references therein). The Kaczawskie Mountains comprise a metamorphosed volcano-sedimentary succession from Cambrian to late Devonian/early Carboniferous and Mesozoic clastic sediments (Mazur et al., 2006; Białek et al., 2007).

SAMPLES AND METHODS

Sample Preparation

Ultramafic mantle xenoliths were collected from an active quarry near Złotoryja city (**Figure 1B**). They were hosted in basanite lavas, and are relatively scarce and typically <5 cm in diameter, although occasionally up to 10 cm. The xenoliths were selected from among the largest unaltered specimens, and then cut, sliced, and polished into 80-μm-thick sections for defining the modal composition, petrography, and mineral chemistry. A suite of samples from the WG quarry was studied and well-characterized by Matusiak-Małek et al. (2017) for major and trace elements, and for Sr and Nd isotopes (see section Petrological Background for details). The present samples are appended with the subscript "II" (e.g., $WG1_{II}$) in order to avoid confusion with the nomenclature adopted by Matusiak-Małek et al. (2017).

Seventeen aliquots of pure and unaltered olivine (Ol), orthopyroxene (Opx), and clinopyroxene (Cpx) were separated for analyzing the noble gases and CO_2 in FI from nine mantle xenoliths. The only exception is for sample $WG5_{II}$ that due to the small dimension of the xenolith was only studied for the modal composition, petrography, and mineral chemistry. After grinding and sieving the rocks, crystals without impurities and larger than 0.5 mm were handpicked under a binocular microscope following the laboratory protocol developed at the Istituto Nazionale di Geofisica e Vulcanologia (INGV), Sezione di Palermo, Italy (e.g., Martelli et al., 2014; Rizzo et al., 2015; Gennaro et al., 2017, and references therein). Aliquots of the minerals were then cleaned ultrasonically in 6.5% HNO_3 before being rinsed with deionized water. The samples were then accurately weighed and loaded into an ultra-high-vacuum crusher for analyses. The amount of loaded sample varied from 0.02 to 1.0 g.

Analytical Procedure

The modal proportion of minerals was determined by point counting, averaging two runs with more than 2,000 points for each thin section (2.5 × 4.0 cm). The smallness of the xenolith samples (5–10 cm) prevented analyses of the bulk major and trace elements, and so the chemical characterization of this xenolith group was based on a detailed *in-situ* investigation.

The major-elements composition of mineral and glass chemistry was determined by a CAMECA SXFive FE electron microprobe equipped with five wavelength-dispersive spectrometers and one energy-dispersive spectrometer at the Department of Lithospheric Research, University of Vienna, Austria. The operating conditions were an accelerating voltage of 15 kV, a beam current of 20 nA, and a counting time 20 s at the peak position. Microscopic images allowed the description of fluid inclusions trapped within single minerals.

The element and isotope composition of noble gases (He, Ne, and Ar) and CO_2 in FI was determined at the laboratories of INGV-Palermo in Italy. The selected crystals were split into two aliquots: the first was loaded into a stainless-steel crusher capable of holding up to six samples simultaneously for noble-gas analysis, and the second was used for determining the concentration and isotope ratio of CO_2. FI were released by in-vacuo single-step crushing at about 200 bar. This conservative procedure was used to minimize the contribution of cosmogenic ^3He and radiogenic ^4He that could possibly have grown or been trapped in the crystal lattice (Kurz, 1986; Hilton et al., 1993, 2002; Rizzo et al., 2015). However, since our samples were collected in a quarry, there should have been no cosmogenic effect. The CO_2 measurement was first performed during noble-gas extraction at the time of crushing by quantifying the total gas pressure (CO_2+N_2+O_2+noble gases) and subtracting the residual pressure of N_2+O_2+noble gases after removing CO_2 using a "cold finger" immersed in liquid N_2 at −196°C. The noble gases were then cleaned in an ultra-high-vacuum (10^{-9}-10^{-10} mbar) purification line, and all species in the gas mixture except for noble gases were removed. He isotopes (^3He and ^4He) and Ne isotopes (^{20}Ne, ^{21}Ne, and ^{22}Ne) were measured separately using two different split-flight-tube mass spectrometers (Helix SFT, Thermo Scientific).

The values of the $^3He/^4He$ ratio are expressed in units of R/Ra, where Ra is the $^3He/^4He$ ratio of air, which is equal to 1.39×10^{-6}. The analytical uncertainty of the He-isotope ratio (1σ) was <3.7%, while this was <2.1 and <4.2% for $^{20}Ne/^{22}Ne$ and $^{21}Ne/^{22}Ne$, respectively. The reported values of both Ne-isotope ratios are corrected for isobaric interferences at m/z values of 20 ($^{40}Ar^{2+}$) and 22 ($^{44}CO_2^{2+}$). Corrections are generally performed by measuring ^{20}Ne, ^{21}Ne, ^{22}Ne, ^{40}Ar, and $^{44}CO_2$ during the same analysis, and considering the previously determined $^{40}Ar^{2+}/^{40}Ar^{+}$ and $^{44}CO_2^{2+}/CO_2^{+}$ ratios on the same Helix SFT that run FI samples. Ar isotopes (^{36}Ar, ^{38}Ar, and ^{40}Ar) were analyzed by a multicollector mass spectrometer (Argus, GVI) with an analytical uncertainty (1σ) of <1.5%. For each analytical session we analyzed at least one standard of each of He, Ne, and Ar that had previously been purified from air and stored in tanks. The analytical uncertainty (1σ) values for the $^3He/^4He$, $^{20}Ne/^{22}Ne$, $^{21}Ne/^{22}Ne$, $^{40}Ar/^{36}Ar$, and $^{38}Ar/^{36}Ar$ ratios were <0.94%, <0.07%, <0.3%, <0.05%, and <0.12%, respectively. The uncertainty in the determinations of the elemental He, Ne, and Ar contents was <5% after considering natural variability and the assumption of residual (not crushed) crystals for weight normalization of the number of moles of gas; typical blanks

for He, Ne, and Ar were $<10^{-15}$, $<10^{-16}$, and $<10^{-14}$ mol, respectively. Further details about the sample preparation and analytical procedures are available in Martelli et al. (2014), Rizzo et al. (2015), and Robidoux et al. (2017).

Our protocol represents the first attempt to estimate the N_2 concentration corrected for atmospheric contamination during the simultaneous extraction of CO_2 and noble gases, which is hereafter reported as N_2^*. We did this by first quantifying ^{40}Ar corrected for air contamination ($^{40}Ar^*$) and then calculating the atmospheric ^{40}Ar present in our samples:

$$^{40}Ar^* = {}^{40}Ar_{sample} - [{}^{36}Ar_{sample} \cdot (^{40}Ar/^{36}Ar)_{air}]$$
$$^{40}Ar_{air} = {}^{40}Ar_{sample} - {}^{40}Ar^*$$

Based on the $O_2/^{40}Ar$ and $N_2/^{40}Ar$ ratios in the atmosphere, we finally calculated the amounts of O_2 and N_2 pertaining to air and subtracted these values from the number of moles of N_2+O_2 measured during extraction. The only assumption was that mantle gases trapped in FI do not contain O_2.

Based on the $^{20}Ne/^{22}Ne$ and $^{21}Ne/^{22}Ne$ ratios (see section Isotope Compositions of He, Ne, Ar, and CO_2 in FI), we corrected ^{21}Ne as follows:

$$^{21}Ne^* = {}^{21}Ne_{sample} - [{}^{22}Ne_{sample} \cdot (^{21}Ne/^{22}Ne)_{air}]$$

Although most of the samples showed a low atmospheric contamination (air has $^4He/^{20}Ne = 0.318$, $^{20}Ne/^{22}Ne = 9.8$, $^{21}Ne/^{22}Ne = 0.029$, and $^{40}Ar/^{36}Ar = 295.5$; Ozima and Podosek, 1983), $^3He/^4He$ was corrected for contamination based on the measured $^4He/^{20}Ne$ ratio as follows:

$$Rc/Ra = ((R_M/Ra)(He/Ne)_M - (He/Ne)_A)/((He/Ne)_M - (He/Ne)_A)$$

where subscripts M and A refer to measured and atmospheric theoretical values, respectively. The corrected $^3He/^4He$ ratios are hereafter reported as Rc/Ra values. However, the correction was either small or negligible for most of the samples, with a maximum bias of ~0.06 Ra for Opx $WG1_{II}$ showing the lowest $^4He/^{20}Ne$ ratio. The CO_2 samples used in the analyses of C isotopes were extracted and quantified in a glass line, which avoids the adsorption and fractionation of CO_2 that can occur in powders and upon contact with stainless steel. We found a very good agreement between the number of moles of CO_2 extracted and quantified in the glass line and that measured during the extraction of noble gases (**Figure S1**). After purification, CO_2 was trapped in a glass sampler and moved to a stable-isotope laboratory for the isotope measurements. Further details about the extraction and analytical protocol can be found in Gennaro et al. (2017). The $^{13}C/^{12}C$ is expressed in delta notation ($\delta^{13}C$) as the difference in parts per mil relative to the V-PDB international standard. The analytical error estimated as 1σ was better than 0.3‰.

PETROLOGICAL BACKGROUND

Xenoliths from WG basanite have been studied by Smulikowski and Kozłowska-Koch (1984) and Matusiak-Małek et al. (2017). They are spinel-bearing peridotites, mostly harzburgites but also some dunites, wehrlites, and clinopyroxenites (**Figure S2**); approximately half of the studied xenoliths contained pargasitic amphibole, but their modal composition and dimensions prevented them from being separated for gas analyses. Xenoliths also contain numerous fine-grained intergranular glassy aggregates (so-called melt pockets). Matusiak-Małek et al. (2017) grouped WG xenoliths based on the chemical composition of Ol into (1) group A, characterized by Ol with $Fo_{89.1-92.5}$, (2) group B, characterized by Ol with $Fo_{85.5-88.1}$, and (3) group C (not described here), characterized by Ol with $Fo_{77.0-82.4}$. The forsterite content of Ol is positively correlated with the Mg# values of pyroxenes (Px) and amphiboles. The entire xenolith suite is interpreted as resulting from a metasomatic reaction between hydrous, CO_2-bearing alkaline silicate melt and a strongly depleted lithospheric mantle. From this viewpoint, group-C xenoliths represent products of reactions involving very high melt/rock ratios, close to that for an open conduit (hydraulic fracturing) system, while group-B and group-A xenoliths record decreasing amounts of melt percolating through and reacting with the refractory mantle. The metasomatic reaction initially enriched the peridotites located close to the source of the agent in Fe and Ti (group B), and the continuum metasomatic interaction introduced Cpx and amphiboles (and possibly also spinel).

TABLE 1 | Textural features and modal composition of Wilcza Góra xenoliths. Modal content of phases by volume percentages.

	Lithology	Texture	Olivine	Orthopyroxene	Clinopyroxene	Spinel	Amphibole
$WG1_{II}$	Harzburgite	protogranular	69.3	27.9	1.0	1.8	-
$WG2_{II}$	Harzburgite	equigranular	63.0	32.8	3.0	1.0	-
$WG3_{II}$	Harzburgite	equigranular	75.0	20.0	2.0	2.0	trace
$WG4_{II}$	Harzburgite	protogranular	60.6	34.1	3.1	2.2	trace
$WG5_{II}$	Harzburgite	porphyroclastic	84.7	13.0	1.7	0.5	trace
$WG6_{II}$	Lherzolite	porphyroclastic	67.1	27.1	5.7	trace	-
$WG7_{II}$	Harzburgite	protogranular	77.6	15.8	3.6	2.3	-
$WG8_{II}$	Harzburgite	porphyroclastic	71.9	25.8	trace	2.3	-
$WG9_{II}$	Lherzolite	protogranular	64.9	27.0	7.6	0.6	-
$WG10_{II}$	Dunite	protogranular	90.9	9.1	trace	trace	trace

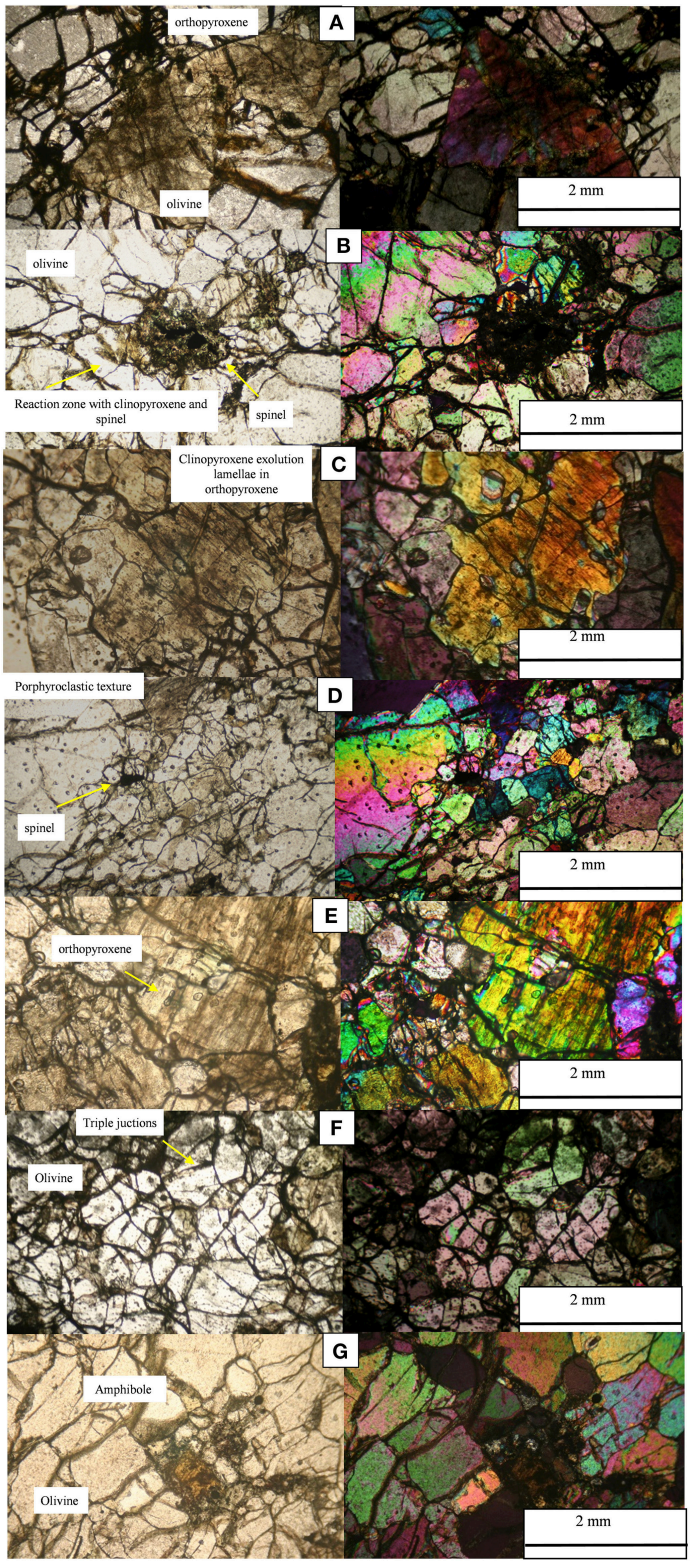

FIGURE 2 | (A–G) Photomicrographs of representative microstructures of WG xenoliths in transmitted plane-polarized light (left) and in cross-polarized light (right). In detail: **(A,B)** images showing protogranular textures with large Opx and Ol grains ($WG4_{II}$); **(B)** a reaction zone with the spongy rims of Cpx and spinel ($WG1_{II}$); **(C)** a protogranular texture with large Opx hosting Cpx exsolution lamellae ($WG9_{II}$); **(D)** examples of porphyroclastic textures with Ol neoblasts slightly oriented and with small Ol replacing large Opx; **(E)** Large opx and small equigranular ol in WGII8; **(F)** Equigranular texture with Ol converging at 120 degrees; **(G)** Small amphiboles associated with the spongy rim of Cpx. Bubbles are evident in Ol ($WG7_{II}$; d).

RESULTS

Petrography

The mantle peridotites are fresh and quite homogeneous. The modal proportion of minerals is presented in **Figure S2** and **Table 1**. The studied samples consist of seven harzburgites, two Cpx-poor lherzolites, and one dunite. The harzburgites contain 85–61 vol.% Ol, 34–13 vol.% Opx, <5 vol.% Cpx, and 1–2.3 vol.% spinel, while the two Cpx-poor lherzolites (Cpx <8 vol.%) contain 67–65 vol.% Ol, around 27 vol.% Opx, and <0.5 vol.% spinel. The dunite mainly consists of Ol (>90 vol.%), with a small amount of Opx (<10 vol.%). These rocks common exhibit a protogranular texture; that is, harzburgites $WG1_{II}$, $WG4_{II}$, and $WG7_{II}$, lherzolite $WG9_{II}$, and dunite $WG10_{II}$. They generally exhibit coarse-grained Opx and Ol (0.6–3 mm; **Figure 2A**); Cpx is smaller (typically 0.4–1 mm) than the other phases and it occurs primarily as a protogranular phase or as nearly formed crystals in the reaction zone (**Figure 2B**). In a few cases ($WG9_{II}$; **Figure 2C**) the Opx core is characterized by Cpx exsolution lamellae. Spinel appears as crystallites associated with a fine-grained reaction zone (**Figures 2B,D**).

Lherzolite $WG6_{II}$ and harzburgites $WG5_{II}$ and $WG8_{II}$ exhibit clearly phorphyroclastic (**Figure 2D**; $WG5_{II}$) textures and generally contain two generations of both Ol and Opx. The large Ol porphyroclasts were subjected to deformation and developed kink bands, whereas the small neoblasts commonly occur as an embayment and partly replace large Opx and Ol porphyroclasts (**Figures 2D,E**). Harzburgites $WG2_{II}$ and $WG3_{II}$ display a well-developed equigranular/granoblastic texture with Ol arranged with a 120° grain-boundary intersection (**Figure 2F**; $WG3_{II}$).

Disseminated amphiboles appear as small anhedral grains that are often associated with the spongy rim of Cpx (**Figure 2G**) or clearly enclose Cpx.

Mineral Chemistry

The mineral chemistry data are reported in **Table 2**. On the basis of Fo [calculated as $Mg/(Mg+Fe_{tot})$ in atoms per formula unit] vs. the distribution of NiO contents, Ol could be divided into two distinct groups: group A (Fo = 89.12–91.48 and NiO = 0.31–0.43 wt.%) and group B (Fo = 85.53–88.13 and NiO = 0.25–0.37 wt.%); this categorization is consistent with groups A and B reported by Matusiak-Małek et al. (2017) (**Figure 3A**).

The two geochemical groups observed in terms of Fo components in Ol are also observed in Px. Opx (En = 85.14–76.85, Fs = 10.07–21.09, and Wo = 1.77–2.04) exhibits a negative correlation between Al_2O_3 contents (1.27–3.31 wt.%) and Mg# values [$Mg/(Mg+Fe_{tot})$ = 86.65–92.05 mol.%; **Figure 3B**], without any significant variation in relation to petrographic features (i.e., Opx in the reaction zone or Opx with exsolution lamellae). Cpx (Wo = 38.52–55.47, En = 52.11–33.91, and Fs = 9.36–10.6) is characterized by a low TiO_2 content (0.02–0.27 wt.%; **Figure S3A**). Samples $WG7_{II}$ and $WG10_{II}$ have slightly elevated TiO_2 (0.66 wt.%), whereas a few of the secondary grains in samples $WG4_{II}$ and $WG6_{II}$ have TiO_2 contents ranging from 1 to 1.20 wt.%. In both Opx and Cpx the Al_2O_3 content (1.43–4.24 wt.%) is negatively correlated with Mg# (87.81–90.84) (**Figure S3B**). Irrespective of the lithology, spinel has Mg# values within the narrow range of 46.94–55.79, while Cr# [= Cr/(Cr+Al) mol.%] values span a larger range (38.88–69.46; **Figure S3C**). The only exception is for sample $WG5_{II}$ that plots out of the mentioned ranges (Mg#=71.63–71.78; Cr#=27.06–27.58; **Figure S3C**).

According to the classification of Leake et al. (1997), the amphiboles are pargasite (samples $WG3_{II}$ and $WG4_{II}$) and ferropargasite (samples $WG5_{II}$ and $WG10_{II}$), whose Mg# values span from 84.63 to 88.88 and their Al_2O_3 and TiO_2 contents are in the ranges of 12.23–13.74 and 0.81–2.85 wt.%, respectively (**Table 2**).

Chemistry of FI

The chemistry of FI hosted in WG xenoliths is reported in **Table 3** and shown in **Figure 4** and **Figure S4**. The gas mixture is dominated by CO_2, which ranges from 0.9×10^{-7} to 24×10^{-7} mol/g (**Figures 4A,B**). N_2 corrected for atmospheric contamination (N_2^*) represents the second major species, whose content varies from 0.86×10^{-9} to 42×10^{-9} mol/g (**Figure 4B**). The atmospheric component in FI, which here is considered to be N_2+O_2+Ar, varies within the same order of magnitude (1.2×10^{-10} to 1.1×10^{-9} mol/g) and with no systematic differences between mineral phases (**Table 3**), and represents <0.3% of the total gas mixture. $^{40}Ar^*$ is within the range of 0.53–7.2×10^{-11} mol/g (**Figures 4C,D**), while ^4He ranges from 0.1×10^{11} to 1.4×10^{11} mol/g (**Figures 4A,C**). The ^{20}Ne concentration ranges from 0.47×10^{-14} to 7.3×10^{-14} mol/g (**Table 3**). Finally, $^{21}Ne^*$ varies from 9.3×10^{-19} to 1.1×10^{-17} mol/g (**Figure S4**).

The average numbers of moles of CO_2, N_2^*, $^{40}Ar^*$, and $^{21}Ne^*$ are higher in Opx than in Ol, which in turn shows a wider compositional range, while the values in Cpx are intermediate (**Figure 4** and **Figure S4**). The only exception is for He, whose content is comparable in Ol and Opx, while it is lowest in Cpx (**Figure 4A** and **Figure S4**). Among Ol, samples $WG4_{II}$, $WG7_{II}$, and $WG10_{II}$ (Fo<88) show the highest concentrations of He and CO_2, and among the largest amounts of N_2^*, $^{40}Ar^*$, and $^{21}Ne^*$. CO_2 is positively correlated with N_2^*, $^{40}Ar^*$, $^{21}Ne^*$, and ^4He (**Figures 4A,B,D** and **Figure S4C**), indicating that the CO_2-rich FI are also rich in the other gas species.

Isotope Compositions of He, Ne, Ar, and CO_2 in FI

The $^3He/^4He$ ratio not corrected for air contamination (R/Ra) is 5.9–6.2 Ra in Ol, 6.1–6.7 Ra in Opx, and 6.7–6.8 Ra in Cpx (**Table 3**). Ol from samples $WG4_{II}$, $WG7_{II}$, and $WG10_{II}$ (Fo < 88) does not show any significant difference in the $^3He/^4He$ ratio. The $^4He/^{20}Ne$ ratio is 163–2125 in Ol, 32–556 in Opx, and 41–176 in Cpx (**Table 3**). The $^{40}Ar/^{36}Ar$ ratio is 818–3,232 in Ol, 1,543–3,007 in Opx, and 1,217–1,270 in Cpx (**Table 2**). The $^{20}Ne/^{22}Ne$ and $^{21}Ne/^{22}Ne$ ratios are 9.9–10.5 and 0.0301–0.0354, respectively, in Ol, 10.0–10.5 and 0.0302–0.0387 in Opx, and 10.1–10.4 and 0.0308–0.0333 in Cpx (**Table 3** and **Figure 5**).

The $^3He/^4He$ ratio corrected for air contamination (Rc/Ra values) is 5.9–6.2 Ra in Ol, 6.1–6.8 Ra in Opx, and 6.7–6.9 Ra in Cpx (**Table 3** and **Figure 6**). It is worth noting that the $^3He/^4He$ ratio increases from Ol to Cpx, with Opx displaying intermediate values (**Figure 6**). This increase is decoupled from the He concentration, since Ol covers the entire range of He contents at almost constant $^3He/^4He$ ratios (6.0 ± 0.1 Ra;

TABLE 2 | Chemistry of minerals forming Wilcza Góra xenoliths.

OLIVINE										
	$WG1_{II}$	$WG2_{II}$	$WG3_{II}$	$WG4_{II}$	$WG5_{II}$	$WG6_{II}$	$WG7_{II}$	$WG8_{II}$	$WG9_{II}$	$WG10_{II}$
Group	A	A	A	B	B	A	B	A	A	B
n.of analyses	5	6	6	7	10	9	7	4	6	5
SiO_2	40.46	40.71	40.29	39.64	39.81	40.61	40.06	40.46	40.28	39.76
TiO_2	0.00	0.00	0.01	0.00	0.01	0.00	0.00	0.00	0.00	0.02
Al_2O_3	0.01	0.01	0.01	0.01	0.02	0.01	0.01	0.01	0.02	0.02
Fe_2O_3										
FeO	9.25	8.50	10.47	12.33	12.92	9.16	11.98	9.25	10.38	13.00
MnO	0.15	0.14	0.17	0.19	0.19	0.15	0.18	0.14	0.15	0.23
MgO	49.60	50.48	48.53	46.87	46.33	49.83	47.29	49.61	48.73	46.75
CaO	0.05	0.05	0.05	0.06	0.06	0.05	0.05	0.05	0.06	0.11
Na_2O										
K_2O										
Cr_2O3	0.02	0.02	0.02	0.01	0.01	0.02	0.01	0.02	0.02	0.02
NiO	0.41	0.40	0.38	0.35	0.32	0.38	0.35	0.40	0.39	0.32
Total	99.95	100.30	99.91	99.47	99.66	100.21	99.94	99.94	100.02	100.22
FeOtot										
Mg#	90.52	91.37	89.20	87.14	86.47	90.65	87.55	90.53	89.32	86.50
Cr#										
A.f.u.										
Si	0.992	0.991	0.994	0.991	0.995	0.993	0.995	0.992	0.992	0.990
Ti										
Al										0.001
FeIII										
FeII	0.190	0.173	0.216	0.258	0.270	0.187	0.249	0.190	0.214	0.271
Mn	0.003	0.003	0.004	0.004	0.004	0.003	0.004	0.003	0.003	0.005
Mg	1.813	1.832	1.784	1.747	1.726	1.815	1.750	1.813	1.789	1.734
Ca	0.001	0.001	0.001	0.002	0.002	0.001	0.001	0.001	0.002	0.003
Na										
K										
Cr										
Ni	0.008	0.008	0.007	0.007	0.006	0.008	0.007	0.008	0.008	0.006
ORTHOPYROXENE										
	$WG1_{II}$	$WG2_{II}$	$WG3_{II}$	$WG4_{II}$	$WG5_{II}$	$WG6_{II}$	$WG7_{II}$		$WG9_{II}$	$WG10_{II}$
	A	A	A	B	B	A	B		A	B
	4	7	3	3	8	4	6		11	3
	56.66	57.87	56.61	56.23	55.32	57.13	56.45		56.62	55.62
	0.02	0.02	0.05	0.15	0.22	0.03	0.08		0.07	0.27
	1.93	1.32	1.86	2.19	3.19	1.71	1.89		2.48	3.00
	0.12	0.02	0.00	0.00	0.02	0.05	0.02		0.01	0.10
	5.77	5.47	7.16	7.81	8.34	5.94	7.51		6.83	8.61
	0.15	0.14	0.18	0.20	0.19	0.15	0.19		0.16	0.23
	34.28	34.93	32.84	32.59	31.75	34.20	32.88		33.34	31.90
	0.67	0.73	0.73	0.77	0.77	0.74	0.79		0.73	0.84
	0.05	0.09	0.09	0.05	0.04	0.07	0.06		0.05	0.05
	0.00	0.00	0.00	0.00	0.00	0.00	0.00		0.00	0.00
	0.51	0.51	0.50	0.46	0.48	0.54	0.40		0.54	0.37
	100.17	101.03	99.39	100.31	100.17	100.34	100.19		100.59	100.96
	5.88	5.49	7.16	7.81	8.36	5.99	7.53		6.85	8.71
	91.22	91.89	89.07	88.15	87.13	91.05	88.62		89.66	86.72
	1.949	1.970	1.973	1.950	1.926	1.963	1.957		1.948	1.924

(Continued)

TABLE 2 | Continued

	0.000	0.001	0.001	0.004	0.006	0.001	0.002	0.002	0.007
	0.078	0.053	0.077	0.090	0.131	0.069	0.077	0.101	0.122
	0.003	0.000	0.000	0.000	0.000	0.001	0.000	0.000	0.003
	0.166	0.155	0.208	0.226	0.242	0.171	0.218	0.196	0.249
	0.005	0.004	0.005	0.006	0.006	0.004	0.006	0.005	0.007
	1.757	1.772	1.705	1.684	1.648	1.751	1.698	1.709	1.645
	0.025	0.027	0.028	0.029	0.029	0.028	0.030	0.027	0.031
	0.003	0.006	0.006	0.003	0.003	0.005	0.004	0.004	0.003
	0.014	0.014	0.014	0.013	0.013	0.014	0.011	0.015	0.010
CLINOPYROXENE									
	$WG1_{I}$	$WG2_{II}$	$WG3_{II}$	$WG4_{II}$	$WG5_{II}$	$WG6_{II}$	$WG7_{II}$	$WG8_{II}$	$WG9_{II}$	WG10II
	A	A	A	B	B	A	B	A	A	B
	3	6	3	1	4	11	6	8	5	4
	53.48	54.72	53.61	50.64	52.06	52.65	53.31	53.25	53.13	52.29
	0.01	0.11	0.13	1.21	0.69	0.36	0.07	0.22	0.21	0.69
	2.91	2.22	2.77	5.05	4.23	3.85	3.17	3.15	3.40	4.17
	0.29	0.14	0.27	0.21	0.20	0.22	0.33	0.17	0.09	0.25
	2.42	2.67	2.64	3.00	3.42	2.88	3.02	2.41	2.78	3.70
	0.08	0.10	0.11	0.10	0.11	0.10	0.11	0.09	0.10	0.15
	16.73	17.82	16.55	16.36	16.02	16.44	16.27	16.61	16.26	16.07
	21.47	19.96	21.45	20.92	21.90	20.78	21.17	21.75	21.67	21.42
	1.06	1.25	1.12	0.68	0.71	1.07	1.18	0.95	0.93	0.84
	1.28	1.74	1.43	1.45	0.87	1.92	1.51	1.50	1.42	1.05
	99.74	100.71	100.08	99.62	100.20	100.26	100.12	100.09	99.95	100.61
	2.68	2.79	2.88	3.19	3.60	3.07	3.31	2.57	2.86	3.92
	91.75	91.97	91.10	90.14	88.80	90.38	89.75	92.02	91.02	87.96
	1.940	1.962	1.942	1.850	1.892	1.906	1.932	1.929	1.930	1.893
	0.001	0.003	0.004	0.033	0.019	0.010	0.002	0.006	0.006	0.019
	0.125	0.094	0.118	0.217	0.181	0.165	0.136	0.135	0.146	0.178
	0.008	0.003	0.008	0.006	0.005	0.006	0.009	0.005	0.002	0.007
	0.073	0.080	0.080	0.092	0.104	0.087	0.091	0.073	0.084	0.112
	0.002	0.003	0.003	0.003	0.004	0.003	0.003	0.003	0.003	0.005
	0.905	0.952	0.893	0.890	0.868	0.886	0.879	0.897	0.880	0.867
	0.835	0.767	0.833	0.819	0.853	0.807	0.822	0.844	0.843	0.831
	0.075	0.087	0.079	0.048	0.050	0.075	0.083	0.067	0.065	0.059
	0.037	0.049	0.041	0.042	0.025	0.055	0.043	0.043	0.041	0.030
SPINEL									
	$WG1_{II}$	$WG2_{II}$	$WG3_{II}$	$WG4_{II}$	$WG5_{II}$		$WG7_{II}$	$WG8_{II}$	$WG9_{II}$	$WG10_{II}$
	A	A	A	B	B		B	A	A	B
	3	5	3	1	2		3	2	3	4
	0.11	0.02	0.02	0.06	0.05		0.04	0.04	0.03	0.10
	0.05	0.07	0.40	0.92	1.01		0.21	0.44	0.34	1.24
	22.08	15.40	18.83	25.12	40.89		21.87	23.62	27.78	30.68
	4.95	4.05	7.20	6.90	6.08		7.36	4.64	4.73	6.17
	12.97	13.79	13.84	15.80	8.38		15.10	12.95	13.69	15.77
	0.33	0.40	0.39	0.10	0.21		0.37	0.34	0.30	0.36
	13.80	12.76	13.32	12.85	19.70		12.49	14.41	14.23	13.57
	0.06	0.01	0.01	0.01	0.27		0.11	0.00	0.04	0.09
	0.00	0.00	0.00							
	0.00	0.00	0.00							
	42.33	51.28	44.17	34.26	22.92		39.82	41.33	36.32	29.17
	0.17	0.15	0.17	0.24	0.30		0.16	0.17	0.17	0.23

(Continued)

TABLE 2 | Continued

	96.85	97.92	98.35	96.26	99.78	97.53	97.92	97.64	97.36
	17.42	17.43	20.32	22.01	13.85	21.72	17.13	17.94	21.32
	58.53	56.61	53.87	51.00	71.71	50.62	59.98	58.57	53.14
	56.25	69.07	61.14	47.78	27.32	54.97	54.00	46.72	38.93
	0.004	0.001	0.001	0.002	0.002	0.001	0.001	0.001	0.003
	0.001	0.002	0.009	0.022	0.021	0.005	0.010	0.008	0.028
	0.820	0.587	0.702	0.934	1.329	0.816	0.861	0.998	1.097
	0.120	0.100	0.170	0.164	0.125	0.173	0.105	0.110	0.140
	0.343	0.372	0.367	0.417	0.195	0.397	0.335	0.350	0.400
	0.009	0.011	0.011	0.003	0.005	0.010	0.009	0.008	0.009
	0.648	0.615	0.628	0.604	0.810	0.589	0.664	0.647	0.614
	0.002	0.000	0.000		0.008	0.004	0.000	0.001	0.003
	0.000	0.000	0.000		0.000	0.000	0.000	0.000	0.000
	0.000	0.000	0.000		0.000	0.000	0.000	0.000	0.000
	1.054	1.310	1.106	0.855	0.500	0.996	1.010	0.875	0.700
	0.005	0.004	0.005		0.007	0.004	0.004	0.004	0.006
AMPHIBOLE									
			$WG3_{II}$	$WG4_{II}$	$WG5_{II}$				$WG10_{II}$
			A	B	B				B
			4	1	5				8
			44.28	43.13	42.56				42.67
			0.83	1.90	2.59				2.76
			12.25	12.84	13.51				13.19
			4.09	4.82	5.02				5.29
			0.08	0.08	0.09				0.10
			18.19	17.30	16.78				16.67
			10.97	11.27	11.50				11.24
			3.20	3.00	2.77				2.90
			0.83	0.89	0.96				0.98
			94.72	95.23	95.77				95.79
			88.79	86.47	85.64				84.89
			6.47	6.308	6.20				6.23
			0.09	0.209	0.28				0.30
			2.11	2.213	2.32				2.27
			0.00	0.000	0.00				0.00
			0.50	0.590	0.61				0.65
			0.01	0.010	0.01				0.01
			3.96	3.772	3.65				3.63
			1.72	1.766	1.80				1.76
			0.91	0.851	0.78				0.82
			0.15	0.167	0.18				0.18

Figure 6A). On the other hand, the $^3He/^4He$ ratios are highest in samples showing the lowest He contents and the largest amounts of CO_2 (**Figure 6B**), N_2^*, $^{40}Ar^*$, and $^{21}Ne^*$ (**Table 3**).

The $\delta^{13}C$ value of mantle CO_2 was determined in most of the mantle xenoliths according to the concentration of CO_2 and the availability of crystals (**Table 3**), with the exception of Cpx from $WG2_{II}$ and $WG8_{II}$, which were not sufficiently abundant to allow further measurements after the noble gases had been measured. $\delta^{13}C$ ranges between −4.2‰ and −3.1‰ in Ol and between −4.7‰ and −3.6‰ in Opx, without any evidence of a correlation with the CO_2 contents (**Figure 7A**). The ratio is slightly less negative for Ol (−3.8 ± 0.4‰) then for Opx (−4.1 ± 0.4‰). $\delta^{13}C$ in Ol was the most negative (−4.2‰) in sample $WG3_{II}$, which also showed the most-negative ratio for Opx (−4.7‰), whereas the least-negative $\delta^{13}C$ was measured in $WG10_{II}$, which did not contain enough Opx for the analysis (**Table 3**).

DISCUSSION

Description of FI

The thin section petrographic observations of the WG mantle xenoliths from which Ol, Opx, and Cpx were separated reveal

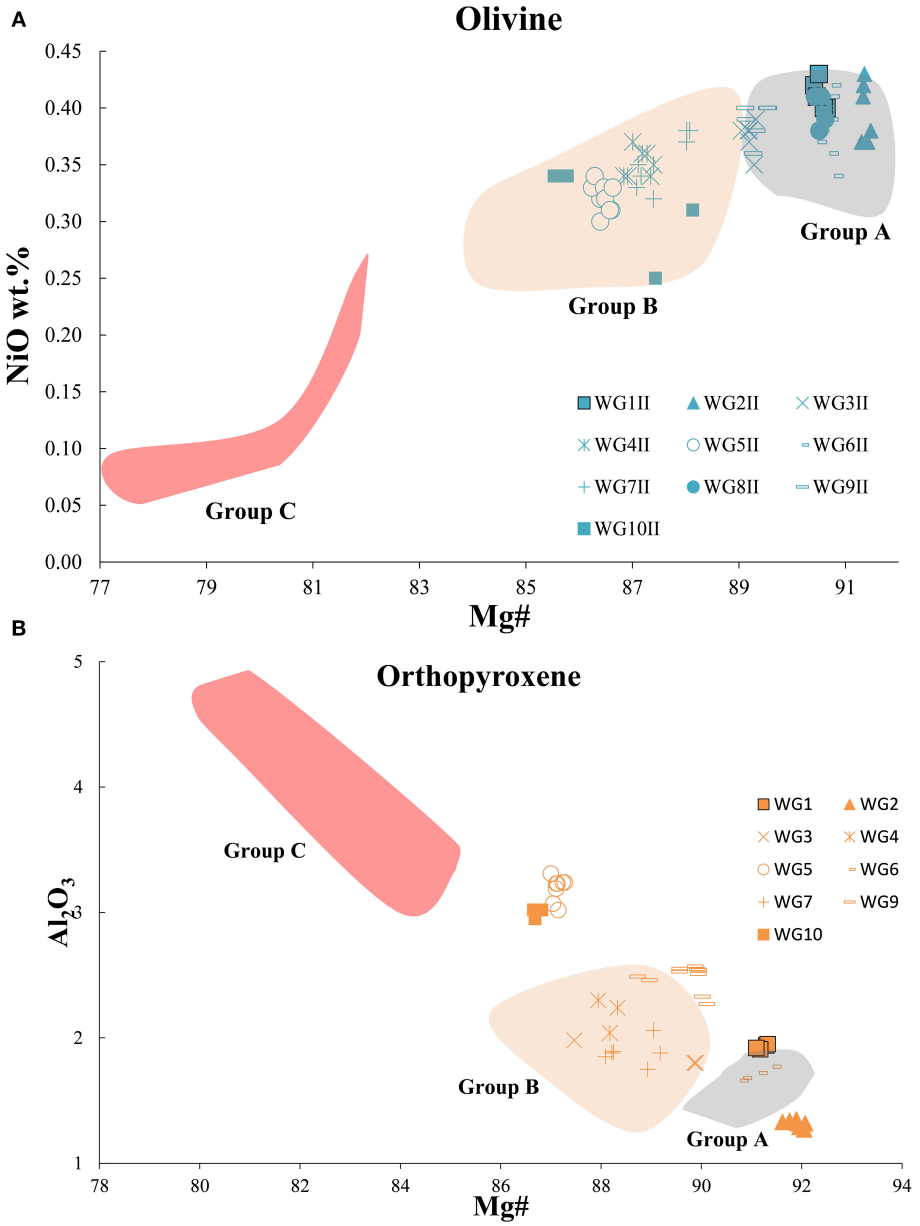

FIGURE 3 | (A) Mg# vs. NiO concentration in Ol. **(B)** Mg# vs. Al_2O_3 in Opx from WG xenoliths. The indicated areas are for the group data reported by Matusiak-Małek et al. (2017).

the clear presence of FI within single crystals (**Figures S5A–D**). These FI have variable dimensions, with the smallest ones being few μm in diameter and the biggest reaching some tens of μm (**Figures S5A–D**). We recognized two types of FI, in accordance with the classification made by Roedder (1984): (1) primary inclusions, present as single inclusions or clusters (**Figures S5A,B**) and/or trails (**Figure S5C**) sometimes developed along plans; (2) secondary inclusions that form clusters and/or trails (**Figure S5D**) mostly developed along plans. The primary inclusions (**Figures S5A–C**) were found always within single coarse grained olivine crystals without continuation to the neighbor grains, an indication that support their primary character (Roedder, 1984); (2) secondary inclusions (**Figure S5D**) form clusters or trails that propagate from clinopyroxene (right part of S5D) to the recrystallized fine grained olivine (left part of S5D). We did not observe FI located along healed fractures. We consider secondary inclusions also trails of FI developed within Cpx and Opx, present e.g., as exsolution lamellae (**Figure S5E**), because trapped after recrystallization due to metasomatic processes.

A detailed study of FI from WG mantle xenoliths was performed by Ladenberger et al. (2009) with similar findings. For this reason, we did not further investigate the morphology and structure of FI from our samples. Importantly, Ladenberger

TABLE 3 | Geochemistry of fluid inclusions hosted in minerals forming mantle xenoliths from Wilcza Góra.

Sample	Mineral	weight (g)	^{4}He mol/g	^{20}Ne mol/g	^{21}Ne mol/g	^{22}Ne mol/g	CO_2	N_2^*	Air mol/g	^{40}Ar mol/g	^{36}Ar mol/g
$WG1_{II}$	Ol	1.01	1.10E-12	5.27E-15	1.61E-17	5.26E-16	8.75E-08	8.62E-10	1.26E-10	6.48E-12	3.95E-15
$WG1_{II}$	Opx	0.30	1.35E-12	4.26E-14	1.28E-16	4.27E-15	5.69E-07	3.91E-09	3.36E-10	1.73E-11	1.06E-14
$WG2_{II}$	Ol	1.00	1.50E-12	9.20E-15	2.81E-17	9.35E-16	1.54E-07	9.38E-10	4.31E-10	1.11E-11	1.36E-14
$WG2_{II}$	Cpx	0.02	1.45E-12	3.54E-14	1.08E-16	3.57E-15	4.25E-07	1.52E-08	8.49E-10	3.40E-11	2.67E-14
$WG2_{II}$	Opx	0.20	2.96E-12	1.86E-14	5.94E-17	1.85E-15	1.25E-06	1.26E-08	7.83E-10	3.81E-11	2.47E-14
$WG3_{II}$	Ol	0.52	2.73E-12	7.05E-15	2.18E-17	6.97E-16	3.21E-07	3.63E-09	3.41E-10	1.38E-11	1.07E-14
$WG3_{II}$	Opx	0.22	5.15E-12	1.40E-14	4.69E-17	1.39E-15	1.75E-06	1.84E-08	5.47E-10	4.53E-11	1.72E-14
$WG4_{II}$	Ol	0.52	1.34E-11	6.29E-15	2.13E-17	6.04E-16	1.12E-06	n.a.	5.71E-10	3.40E-11	1.80E-14
$WG4_{II}$	Ol	0.12	2.56E-12	9.69E-15	3.09E-17	9.44E-16	1.36E-06	1.58E-08	3.85E-10	3.64E-11	1.21E-14
$WG4_{II}$	Opx	0.10	7.27E-12	7.33E-14	2.20E-16	7.27E-15	2.42E-06	1.75E-08	1.06E-09	8.14E-11	3.33E-14
$WG6_{II}$	Ol	1.06	4.89E-12	4.72E-15	1.53E-17	4.59E-16	3.41E-07	1.94E-09	3.54E-10	1.71E-11	1.11E-14
$WG6_{II}$	Opx	0.05	3.68E-12	9.28E-15	2.85E-17	9.22E-16	3.44E-07	n.a.	1.30E-10	1.32E-11	4.09E-15
$WG7_{II}$	Ol	1.02	6.24E-12	7.65E-15	2.35E-17	7.59E-16	3.60E-07	2.99E-09	3.41E-10	1.69E-11	1.07E-14
$WG7_{II}$	Opx	0.03	4.13E-12	3.54E-14	1.11E-16	3.48E-15	1.83E-06	1.19E-08	5.93E-10	4.67E-11	1.87E-14
$WG8_{II}$	Ol	0.51	1.43E-11	4.32E-14	1.30E-16	4.34E-15	1.91E-06	7.91E-09	4.66E-10	4.29E-11	1.47E-14
$WG8_{II}$	Cpx	0.04	8.60E-13	4.90E-15	1.56E-17	4.78E-16	4.50E-07	7.31E-09	5.61E-10	2.15E-11	1.77E-14
$WG8_{II}$	Opx	0.10	5.04E-12	3.96E-14	1.20E-16	3.91E-15	2.35E-06	4.24E-08	7.65E-10	5.67E-11	2.41E-14
$WG9_{II}$	Ol	1.02	2.65E-12	6.92E-15	2.16E-17	6.88E-16	3.01E-07	1.48E-09	1.98E-10	1.06E-11	6.25E-15
$WG9_{II}$	Opx	0.29	2.50E-12	7.03E-15	2.28E-17	6.62E-16	1.04E-06	6.99E-09	5.56E-10	3.79E-11	1.75E-14
$WG10_{II}$	Ol	0.90	8.58E-12	6.06E-15	1.86E-17	5.90E-16	7.73E-07	2.96E-09	9.48E-10	3.18E-11	2.99E-14
$WG10_{II}$	Opx	0.07	2.97E-12	5.35E-15	1.96E-17	5.12E-16	1.25E-06	1.07E-08	4.83E-10	3.44E-11	1.52E-14

^{40}Ar* mol/g	^{4}He/^{20}Ne	^{4}He/^{40}Ar*	^{4}He/N_2^*	^{4}He/CO_2	CO_2/N_2^*	CO_2/Ar*	Ar*/N_2^*	R/Ra	Rc/Ra	Err Rc/Ra +/ −	^{40}Ar/^{36}Ar
5.31E-12	209.1	0.21	1.28E-03	1.26E-05	101.58	1.65E+04	6.16E-03	5.92	5.93	0.07	1638.81
1.42E-11	31.7	0.10	3.45E-04	2.38E-06	145.34	4.00E+04	3.63E-03	6.71	6.77	0.08	1639.95
7.10E-12	163.4	0.21	1.60E-03	9.78E-06	163.82	2.16E+04	7.57E-03	5.90	5.91	0.06	818.33
2.61E-11	41.2	0.06	9.59E-05	3.42E-06	28.03	1.63E+04	1.72E-03	6.85	6.90	0.26	1270.54
3.08E-11	159.5	0.10	2.35E-04	2.37E-06	99.51	4.07E+04	2.45E-03	6.54	6.55	0.08	1543.41
1.06E-11	386.9	0.26	7.52E-04	8.51E-06	88.34	3.02E+04	2.93E-03	6.18	6.18	0.06	1283.53
4.02E-11	368.8	0.13	2.81E-04	2.94E-06	95.44	4.35E+04	2.19E-03	6.27	6.28	0.07	2631.27
2.87E-11	2125.5	0.47	n.a.	1.20E-05	n.a.	3.90E+04	n.a.	5.95	5.95	0.05	1890.39
3.29E-11	264.0	0.08	n.a.	1.89E-06	n.a.	4.13E+04	n.a.	6.11	6.12	0.07	3007.12
7.16E-11	99.2	0.10	4.15E-04	3.01E-06	138.19	3.38E+04	4.09E-03	6.30	6.32	0.09	2445.01
1.38E-11	1035.5	0.35	2.52E-03	1.43E-05	175.35	2.47E+04	7.09E-03	5.88	5.88	0.06	1532.60
1.20E-11	396.3	0.31	n.a.	1.07E-05	n.a.	2.86E+04	n.a.	5.90	5.91	0.06	3232.38
1.38E-11	815.4	0.45	2.09E-03	1.73E-05	120.29	2.61E+04	4.61E-03	5.93	5.93	0.05	1579.12
4.12E-11	116.7	0.10	3.47E-04	2.25E-06	153.90	4.45E+04	3.46E-03	6.60	6.61	0.09	2500.22
3.85E-11	331.5	0.37	1.81E-03	7.50E-06	241.46	4.95E+04	4.87E-03	6.07	6.07	0.06	2921.35
1.63E-11	175.6	0.05	1.18E-04	1.91E-06	61.51	2.76E+04	2.23E-03	6.66	6.67	0.20	1217.14
4.96E-11	127.3	0.10	1.19E-04	2.14E-06	55.43	4.74E+04	1.17E-03	6.06	6.08	0.08	2354.55
8.79E-12	383.6	0.30	1.79E-03	8.82E-06	203.16	3.42E+04	5.94E-03	5.94	5.94	0.09	1702.90
3.27E-11	355.2	0.08	3.57E-04	2.40E-06	149.10	3.18E+04	4.69E-03	6.26	6.26	0.12	2163.75
2.30E-11	1416.6	0.37	2.90E-03	1.11E-05	261.65	3.37E+04	7.77E-03	6.08	6.08	0.06	1064.79
2.99E-11	555.6	0.10	2.77E-04	2.38E-06	116.24	4.17E+04	2.79E-03	6.39	6.39	0.07	2260.23

(Continued)

TABLE 3 | Continued

Err (%)	$^{38}Ar/^{36}Ar$	Err (%)	$^{20}Ne/^{22}Ne$	Err 20/22 +/−	$^{21}Ne/^{22}Ne$	Err 21/22 +/−	^{3}He	$CO_2/^{3}He$	$^{\#}CO_2$	$\delta^{13}C$ ‰ VPDB
0.06	0.18630	0.19	10.07	0.02	0.0308	0.00032	9.08E-18	9.64E+09	n.a.	n.a.
0.07	0.18893	0.19	10.01	0.02	0.0302	0.00023	1.27E-17	4.48E+10	*3.66E-07*	−3.6
0.72	0.18708	0.19	9.87	0.02	0.0301	0.00022	1.24E-17	1.24E+10	1.58E-07	−3.8
0.33	0.18697	0.19	10.07	0.09	0.0308	0.00127	1.40E-17	3.05E+10	n.a.	n.a.
1.12	0.18940	0.19	10.15	0.02	0.0325	0.00053	2.70E-17	4.64E+10	*3.73E-07*	−4.1
0.05	0.18470	0.18	10.14	0.03	0.0315	0.00040	2.35E-17	1.37E+10	2.33E-07	−4.2
0.09	0.19146	0.19	10.15	0.03	0.0342	0.00042	4.50E-17	3.89E+10	1.41E-06	−4.7
0.94	0.18938	0.19	10.47	0.03	0.0354	0.00067	1.11E-16	1.01E+10	1.40E-06	−4.1
0.21	0.19221	0.19	10.23	0.07	0.0326	0.00140	2.18E-17	6.24E+10	n.a.	n.a.
0.13	0.18869	0.19	10.14	0.03	0.0305	0.00048	6.39E-17	3.79E+10	1.13E-06	−4.1
0.76	0.18676	0.19	10.30	0.02	0.0334	0.00053	3.99E-17	8.53E+09	5.55E-07	−3.9
0.08	0.18852	0.19	10.09	0.02	0.0310	0.00043	3.02E-17	1.14E+10	3.20E-07	−3.8
0.73	0.18825	0.19	10.12	0.02	0.0311	0.00041	5.14E-17	6.99E+09	4.34E-07	−4.0
0.09	0.19080	0.19	10.22	0.03	0.0322	0.00041	3.80E-17	4.82E+10	1.15E-06	−4.0
0.11	0.18788	0.19	10.05	0.02	0.0302	0.00036	1.21E-16	1.58E+10	n.a.	n.a.
0.24	0.18589	0.19	10.41	0.22	0.0333	0.00141	7.97E-18	5.64E+10	n.a.	n.a.
0.09	0.18628	0.19	10.10	0.02	0.0307	0.00052	4.25E-17	5.53E+10	n.a.	n.a.
1.32	0.18299	0.18	10.08	0.02	0.0315	0.00034	2.19E-17	1.37E+10	*4.17E-07*	−4.0
0.28	0.18860	0.19	10.58	0.17	0.0344	0.00271	2.17E-17	4.79E+10	n.a.	n.a.
0.38	0.18335	0.18	10.35	0.01	0.0319	0.00121	7.25E-17	1.07E+10	2.13E-07	−3.1
1.55	0.18960	0.19	10.52	0.06	0.0387	0.00074	2.64E-17	4.72E+10	n.a.	n.a.

Ol stands for olivine, cpx for clinopyroxene, and opx for orthopyroxene. $^{\#}$Indicates CO_2 measured from glass line. Among these measurements, those reported in italics and underlined are single analysis while the other represent average of two or more replicates.

et al. (2009) inferred that FI were formed under upper-mantle conditions, which supports the reliability of information on mantle features and processes obtained in the present work.

Petrological Evidence of the Type and Timing of Processes Modifying Local Mantle

The textural features and chemistry of major mineral phases of WG mantle xenoliths provide important evidence of the type and timing of processes that acted in modifying the local mantle before the mantle xenoliths were brought to the surface. In a hypothetical melting trend, fusible elements (Ti and Al) tend to decrease with increasing Mg# (Ionov and Hofmann, 2007; Bonadiman and Coltorti, 2011). We estimated the degree of melting of WG mantle based on the contents of Al_2O_3 vs. MgO in primary Opx (**Figure S6**) following the model of Upton et al. (2011). Comparing our results with those of Matusiak-Małek et al. (2017) confirms that WG xenoliths record a residual mantle that is strongly depleted after 25–30% of partial melting (**Figure S6**).

The textural characteristics (i.e., secondary Px and the presence of amphiboles; **Figure 3**) and geochemical characteristics (i.e., TiO_2 enrichment in Cpx; **Figure S3**) of the group-A and group-B xenoliths provide evidence of peridotite–melt interaction. This evidence is in accordance with the findings of Matusiak-Małek et al. (2017), who suggested that Ol from group-A xenoliths represent the residuum after partial melting. Instead, Cpx is clearly metasomatized, and consequently the FI entrapped by this mineral are secondary (**Figure S5D**) and inherited by the metasomatic agent (see section Mantle Metasomatism). Opx, which exhibits petrographic and mineral chemistry evidence of recrystallization, is at least partially modified by metasomatic interactions. Based on these evidence we argue that the residual mantle was subsequently modified by metasomatic processes.

Finally, the presence of amphiboles, sometimes enclosing Cpx, suggests the introduction of hydrous fluids that could originate from a previous (fossil) subduction, as proposed by the model of Faccenna et al. (2010).

Processes That Modify the Geochemistry of FI

Atmospheric Contamination

While the atmospheric concentration of He is relatively low, the heavy noble gases have accumulated during the evolution of the Earth and so are more prone to contamination. This process can partially or completely mask the original signature recorded by the minerals. The systematics of Ne and Ar isotopes (and complementarily the $^{4}He/^{20}Ne$ ratio) in WG xenoliths highlight the air contamination in FI, resulting in a mixing between mantle- and atmosphere-derived noble gases (**Table 3**). The plot of the three Ne isotopes in **Figure 5** shows that our data fall

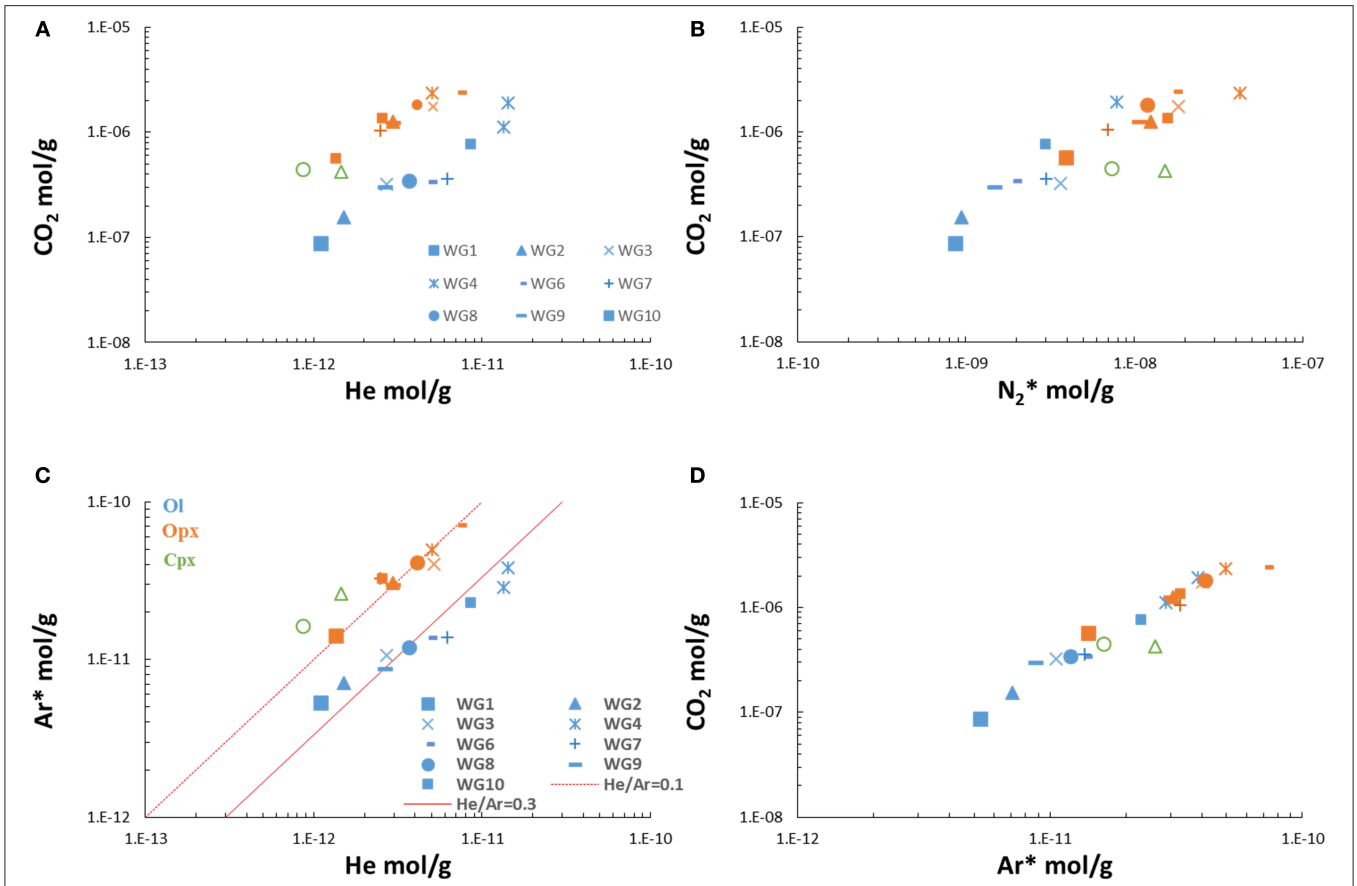

FIGURE 4 | Elemental concentrations measured in FI after single-step crushing of CO_2 vs. **(A)** He, **(B)** N_2^*; diagram of concentrations of Ar* vs. **(C)** He and **(D)** CO_2.

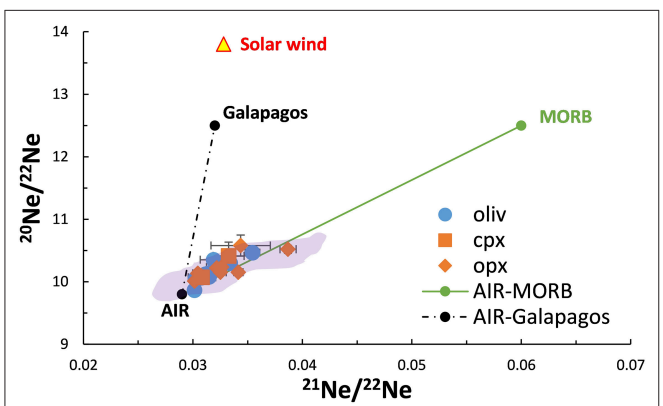

FIGURE 5 | Diagram of $^{21}Ne/^{22}Ne$ vs. $^{20}Ne/^{22}Ne$. The green line represents binary mixing between air and a MORB mantle as defined by Sarda et al. (1988) and Moreira et al. (1998) at $^{21}Ne/^{22}Ne = 0.06$ and $^{20}Ne/^{22}Ne = 12.5$. The black dotted line indicates binary mixing between air and the OIB domain of the Galapagos Islands as determined by Kurz et al. (2009) at $^{21}Ne/^{22}Ne = 0.032$ and $^{20}Ne/^{22}Ne = 12.5$. The primordial neon composition is also reported as Solar wind (e.g., Heber et al., 2009), with at $^{21}Ne/^{22}Ne = 0.0328$ and $^{20}Ne/^{22}Ne = 13.8$. The violet area indicates data from other European localities (French Massif Central, Eifel, and Pannonian Basin) measured by Gautheron et al. (2005).

along the theoretical mixing line between air and a MORB-like mantle, defined by Sarda et al. (1988) and Moreira et al. (1998) at $^{21}Ne/^{22}Ne = 0.06$ and $^{20}Ne/^{22}Ne = 12.5$. Similarly, $^{40}Ar/^{36}Ar$ values are well below the theoretical ratio in the mantle ($^{40}Ar/^{36}Ar$ up to 44,000; e.g., Burnard et al., 1997; Moreira et al., 1998) or typical mantle-derived samples (e.g., Kaneoka, 1983; Ozima and Podosek, 1983; Allègre et al., 1987), confirming the presence of a certain amount of contamination by atmosphere-derived fluids. Such evidence has also been found in other European as well as worldwide SCLM xenoliths (Valbracht et al., 1996; Matsumoto et al., 1998, 2000, 2001, 2002; Yamamoto et al., 2004; Gautheron et al., 2005; Martelli et al., 2011; Correale et al., 2012, 2016).

Several hypotheses were invoked to explain the presence of air in FI as indicated by the Ne- and Ar-isotope data from mantle xenoliths: (1) contamination of the xenoliths as they are brought from the mantle to the surface, caused by the percolation of melts or volatiles in the xenoliths (i.e., Buikin et al., 2005; Gautheron et al., 2005), (2) air entrapment in microcracks of the minerals during or after the eruptive activity (i.e., Martelli et al., 2011; Correale et al., 2012), and (3) mantle contamination at depth from the dehydration of atmospheric gases from subducting oceanic crust (i.e., Matsumoto et al., 1998, 2000, 2001; Yamamoto

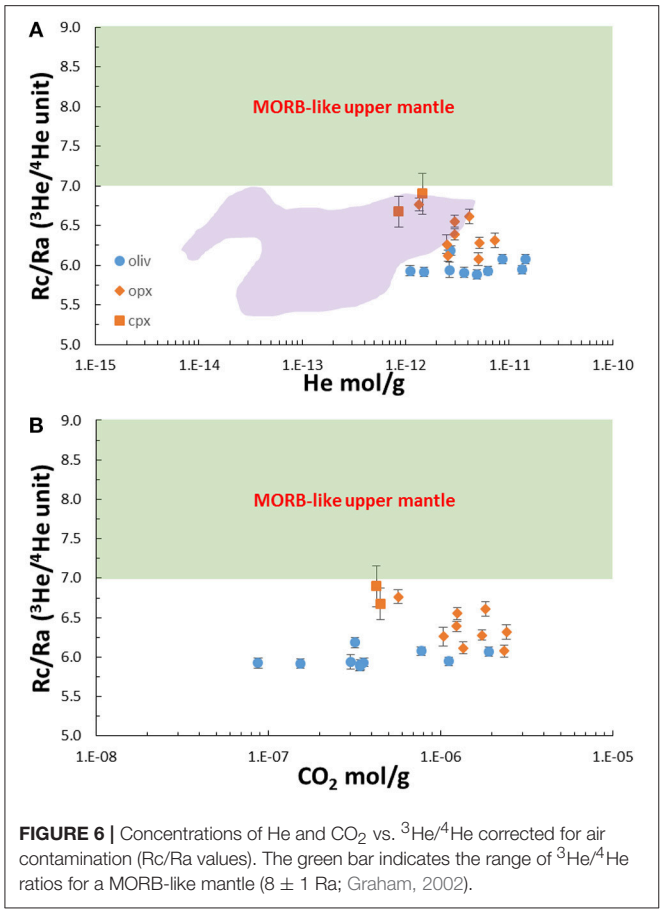

FIGURE 6 | Concentrations of He and CO_2 vs. ^{3}He/^{4}He corrected for air contamination (Rc/Ra values). The green bar indicates the range of ^{3}He/^{4}He ratios for a MORB-like mantle (8 ± 1 Ra; Graham, 2002).

et al., 2004; Gurenko et al., 2006). Our observations make the first two hypotheses unlikely because we found no difference between Ol and Px, with the latter having entrapped FI related to the metasomatic agent (see section Mantle Metasomatism). In addition, detailed observations of Ol and Px did not produce any evidence of microcracks, since their presence would have produced systematic differences between the analyzed minerals. We therefore consider the third hypothesis to be the most reasonable, although there is no evidence of a recent subduction in this part of Europe, with the last subduction event dated to the Ordovician-Devonian period (Kryza et al., 2011). More likely, the recent model proposed by Faccenna et al. (2010 and references therein) proposes that slab fragmentation within the upper mantle may influence outside-arc alkaline magmatism generated both ahead of the slab in the back-arc region and around the lateral edges of the slab. In fact, other geochemical tracers in erupted rocks (Sr, Nd, and Pb isotopes; Lustrino and Wilson, 2007) provide evidence for the recycling of subduction-related volatiles in the European mantle.

The most widely accepted model for explaining the noble-gas geochemistry of SCLM assumes a type of steady state resulting from the mixing between fluids infiltrating from the asthenosphere and those already present in the lithosphere and originating from the recycling of crustal- and atmosphere-derived noble gases introduced from past subduction events into the European mantle (Gautheron and Moreira, 2002; Gautheron et al., 2005). In the case of WG mantle xenoliths, the presence of amphiboles could indicate the presence of hydrous fluids originating from a previous (fossil) subduction event, in accordance with the model proposed by Faccenna et al. (2010).

As is the case in subduction-related settings (i.e., arc volcanoes), Ne- and Ar-isotope ratios are systematically lower and close to theoretical values in the atmosphere (Hilton et al., 2002; Martelli et al., 2014; Di Piazza et al., 2015; Rizzo et al., 2015; Robidoux et al., 2017; Battaglia et al., 2018), irrespective of whether Ol phenocrysts or mantle xenocrysts are analyzed.

Diffusive Fractionation of He

The clearest evidence from the chemistry of FI is that the He/CO_2, He/^{40}Ar*, He/N_2^*, and He/^{21}Ne* (not shown) ratios are systematically lower in Cpx and Opx than in Ol (**Figures 8A,B**). This pattern is not observed for ratios that do not include He [i.e., CO_2/^{40}Ar*, ^{40}Ar*/N_2^*, and ^{21}Ne*/N_2^* (not shown); **Figure 8C**], which show at least a partial overlapping of data among Ol and Px. This difference might originate from the diffusive loss of He from mantle minerals (e.g., Burnard et al., 1998 and references therein), which increases from Ol to Cpx. This hypothesis is supported by the diffusion coefficient (D) being significantly higher for He than for the other noble gases (e.g., $D_{4He}/D_{40Ar} = 3.16$ in solid mantle; Burnard, 2004; Yamamoto et al., 2009), N_2^*, and CO_2.

Figure 9 plots He/^{40}Ar* and He/CO_2 vs. the He concentration to determine if the decreases in these ratios are associated with a clear decrease in the He concentration, as expected if partial loss occurs. Such a tendency is clearer for Ol than for Px, while it is less evident or absent for He/CO_2 vs. He (**Figure 9**). In the case of the diffusive loss of He, we should also expect an isotope fractionation of ^{3}He/^{4}He due to the appreciable difference in D_{3He} and D_{4He} among mantle minerals that is proportional to the atomic mass ($D_{3He}/D_{4He} = 1.15$; Trull and Kurz, 1993; Burnard, 2004; Yamamoto et al., 2009 and references therein.). However, plotting the He concentration vs. Rc/Ra (**Figure 6A**) for Ol reveals no obvious variations of the ^{3}He/^{4}He ratio for decreasing He, with the isotope ratio varying over a very narrow range (5.9–6.2 Ra). Moreover, Opx and Cpx display higher ^{3}He/^{4}He ratios (6.3–6.9 Ra) than Ol for comparable He contents. This behavior is the opposite of what would be expected in the presence of He diffusive loss (e.g., Burnard, 2004; Harrison et al., 2004; Nuccio et al., 2008), as also suggested by plots of He/^{40}Ar*, He/^{21}Ne* (not shown), He/N_2^* (not shown), and He/CO_2 vs. Rc/Ra (**Figures 10A,B**).

Together these observations indicate that the observed data variability cannot be explained by a partial loss of He. A process of diffusive fractionation of noble gases within the mantle can also be excluded because this would lead to decreases in both He/^{40}Ar* and ^{3}He/^{4}He (Yamamoto et al., 2009). Finally, diffusive fractionation cannot explain our data irrespective of the assumed starting conditions. If this process had occurred in Ol and Px, it would be successively erased by the new injection of trapped fluids, especially within Px (see section Mantle Metasomatism).

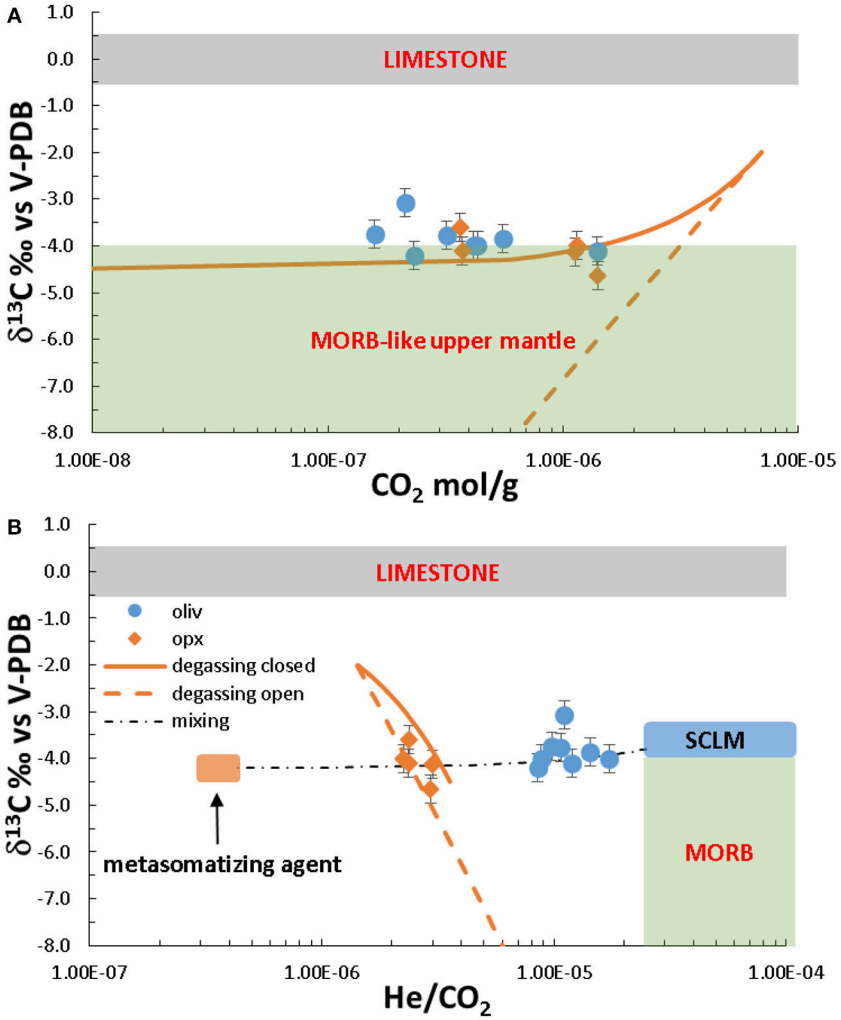

FIGURE 7 | (A) CO_2 concentration and **(B)** He/CO_2 vs. the C-isotope composition ($\delta^{13}C$ relative to V-PDB) in FI. The green bar [and rectangle in **(B)**] indicates the range of $\delta^{13}C$ values for a MORB-like mantle ($-8‰ < \delta^{13}C < -4‰$; Sano and Marty, 1995), while the gray bar is for limestone ($-1‰ < \delta^{13}C < +1‰$; Sano and Marty, 1995). The orange solid line indicates a closed-system equilibrium degassing path [equation from Jambon et al. (1986) and Macpherson and Mattey (1994)], while the orange dashed line indicates an open-system equilibrium degassing path (equation from Hoefs, 2015). The following starting conditions were assumed for degassing modeling: $CO_2 = 7 \times 10^{-6}$ mol/g, $He = 2.5 \times 10^{-11}$ mol/g, $\delta^{13}C = -4.5‰$, and $\varepsilon_{vap-melt} = 2.5‰$ (Mattey, 1991), solubility of $CO_2 = 7.6 \times 10^{-4}$ cc STP/g/bar (taken from Guillot and Sator, 2011) at 2 GPa and 1,673°K, and solubility of $He = 1.9 \times 10^{-3}$ cc STP/g/bar [assumed considering a He/CO_2 ($\alpha_{He,CO2}$) solubility ratio of 2.5 as indicated by Hilton et al. (1997), Barry et al. (2014), and Gennaro et al. (2017)]. The black dotted line in **(B)** represents binary mixing between two endmembers: (1) the residual mantle (blue rectangle) having $He/CO_2 = 2.5 \times 10^{-5}$ and $\delta^{13}C = -3.5‰$, and (2) the metasomatic agent (orange rectangle) having $He/CO_2 = 3.7 \times 10^{-7}$ and $\delta^{13}C = -4‰$.

Partial Melting of the Mantle

Plotting $He/^{40}Ar^*$ vs. the $^{40}Ar^*$ concentration (**Figure 11A**) and He/CO_2 vs. the CO_2 concentration (**Figure 11B**) reveals that the decreases in these ratios within Ol are accompanied by decreases in the absolute concentrations (although this is less clear for CO_2), as observed when plotting vs. the He concentration (see section Diffusive Fractionation of He and **Figures 9A,B**). This suggests that the process responsible for the variability within Ol modified the entire chemistry of FI. On the other hand, the decrease in these ratios from Ol to Cpx is associated with either no change or only a slight increase in the mean concentration of each species (**Figures 9**, **11**). We argue that the decreases in these ratios among Ol and Px are not caused by the same process underlying the variability in Ol, and also that the timing of the processes is probably different (see section Mantle Metasomatism). We therefore focus on the effect that partial melting has on the chemistry of FI within Ol resembling the residual mantle. This is supported by the evidence from petrography and mineral chemistry (see section Petrological Evidence of the Type and Timing of Processes Modifying Local Mantle) indicating that Ol with Fo>89 can be considered as a residuum from the partial melting of lithospheric

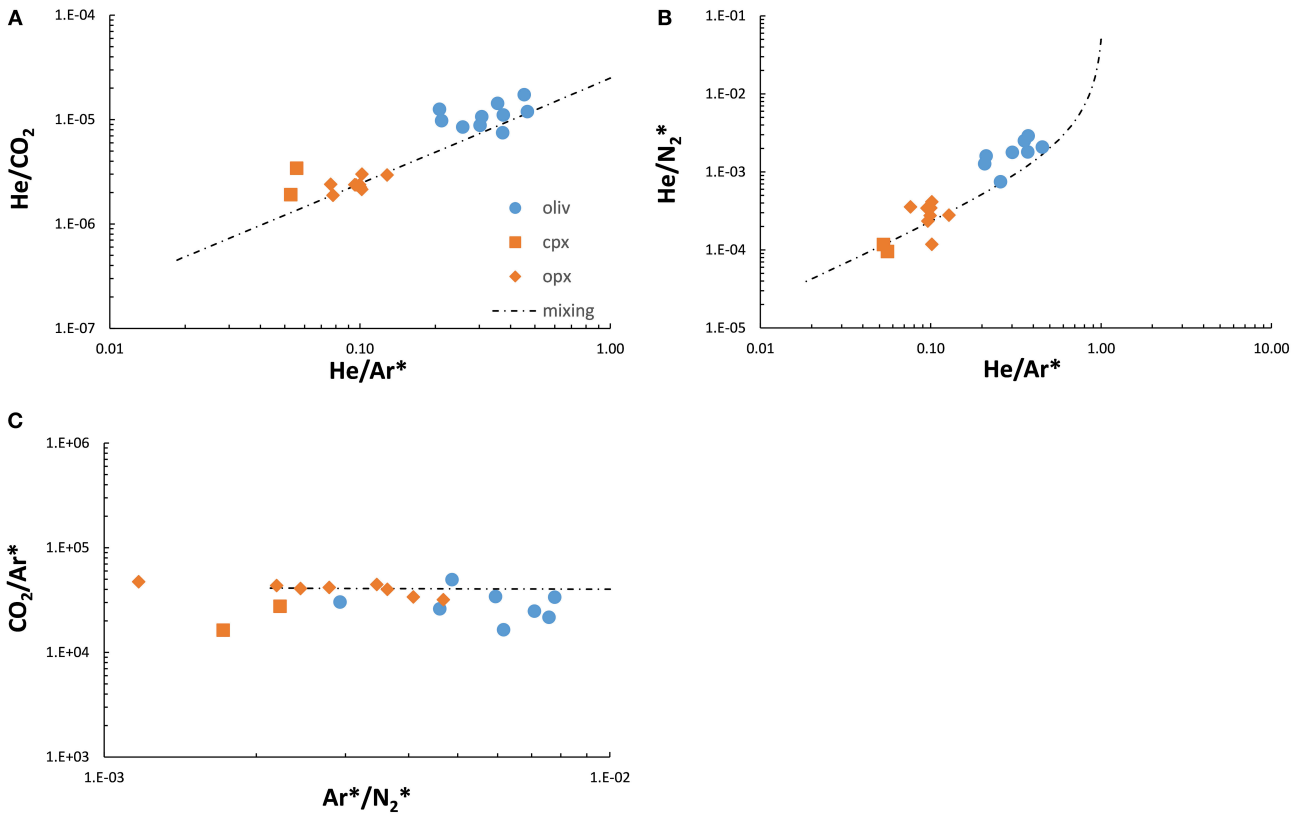

FIGURE 8 | He/Ar* vs. **(A)** He/CO_2 and **(B)** He/N_2^*, and **(C)** Ar^*/N_2^* vs. CO_2/Ar^* in FI. The black dotted line represents binary mixing between two endmembers: (1) the residual mantle having $He/Ar^* = 1$, $He/CO_2 = 2.5 \times 10^{-5}$, $He/N_2^* = 5 \times 10^{-2}$, $Ar^*/N_2^* = 5 \times 10^{-2}$, and $CO_2/Ar^* = 4 \times 10^4$, and (2) the metasomatic agent having $He/Ar^* = 1.7 \times 10^{-2}$, $He/CO_2 = 3.7 \times 10^{-7}$, $He/N_2^* = 3.7 \times 10^{-5}$, $Ar^*/N_2^* = 2.1 \times 10^{-3}$, and $CO_2/Ar^* = 4.7 \times 10^4$. These two endmembers were assumed based on the minimum and maximum concentrations of single species in the three mineral phases and in order to fit the entire data set.

mantle (Matusiak-Małek et al., 2017; **Table 2**). Ol from samples $WG4_{II}$, $WG7_{II}$, and $WG10_{II}$ show Fo<89 and could have been partially influenced by metasomatic process leading to partial recrystallization and thus entrapment of new FI (see section Mantle Metasomatism). In this view the $^3He/^4He$ ratio does not show any relation with the forsterite content (**Figure S7**), while $He/^{40}Ar^*$ decreases slightly at Fo>89 and reflects increasing extents of partial melting.

Assuming the presence of crystal–melt partitioning of noble gases for Ol and Cpx (Heber et al., 2007), we modeled the trend of partial melting for batch and fractional melting of mantle in the spinel stability field. For the starting composition in the crystal, we assumed $He = 5 \times 10^{-11}$ mol/g, $Ar^* = 4 \times 10^{-11}$ mol/g, and $CO_2 = 1.5 \times 10^{-6}$ mol/g. Briefly, we chose to use the highest Ar^* and CO_2 concentrations measured in Ol, while the He content was chosen so that the $He/^{40}Ar^*$ ratio was within the reported range for mantle production ($He/^{40}Ar^* = 1$–5; Marty, 2012). We considered the He and $^{40}Ar^*$ concentrations vs. $He/^{40}Ar^*$ (**Figures 9**, **11**), for which partitioning coefficients are known and more data are available in the literature for similar applications elsewhere (e.g., Burnard, 2004; Yamamoto et al., 2009). A particularly interesting observation was that the batch equilibrium melting trend fits most of the Ol data, especially those with Fo>89, whereas Px cannot be explained by this process. The chemical variation of FI within Ol traces the partial melting trend, and this is in accordance with the main lithophile-elements-based melting models (Matusiak-Małek et al., 2017; present study). However, estimations of the degree of melting based on noble-gas modeling yield much lower percentages (<1%) than the common petrological estimations (20–30% melt; **Figure S6**). This large discrepancy could be due to us measuring noble gases in the FI, while partitioning coefficients are given for a crystal–melt. In other words, we did not measure noble gases in the crystal lattice where we should expect that our estimations match those of lithophile-elements-based melting models. We argue that there is a general equilibrium between FI and the crystal lattice, and this explains why noble gases (and their relative ratios) follow the partial melting trend. In any case we use our tracers only as a proxy for the occurrence of partial melting, and not to speculate about the extent of this process.

Mantle Metasomatism

While the geochemistry of FI in Ol reflects variable extents of partial melting, that of Cpx and (at least partially) Opx cannot be explained by this process, and suggests a contribution

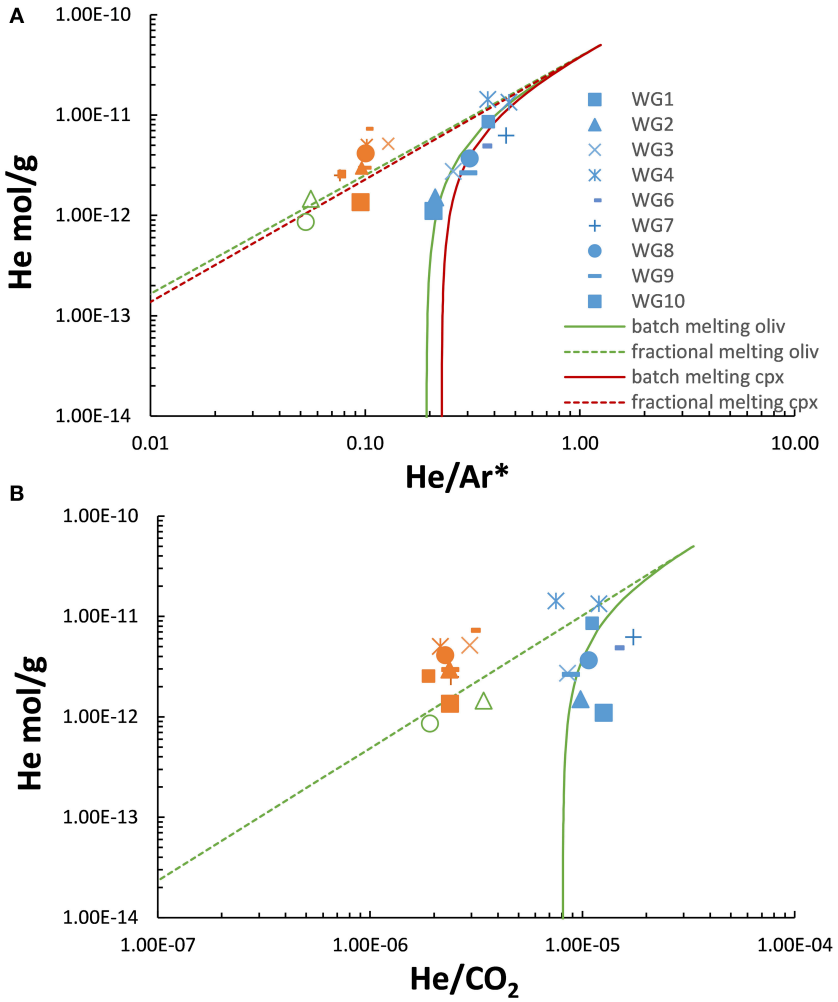

FIGURE 9 | (A) He/Ar* and **(B)** He/CO_2 vs. the He concentration. Modal batch and fractional equilibrium melting were modeled using the following equations:

$$C_i^m = \frac{C_i^s}{\left[F + D_i^{\frac{cryst}{melt}} \cdot (1-F)\right]} \; batch\ melting \ldots\ldots C_i^m = \left[C_i^s \cdot \left(\frac{1}{D_i^{\frac{cryst}{melt}}} \right) \cdot (1-F)^{\left(\frac{1}{D_i^{\frac{cryst}{melt}}} - 1 \right)} \right] \; fractional\ melting$$

where C_i^m and C_i^s are the concentrations of the *i*th species in the melt and solid source, respectively; *F* is the melting fraction, which varies from 0 to 1; and $D_i^{\frac{cryst}{melt}}$ is the crystal–melt partitioning coefficient of the *i*th species. The coefficients for the crystal–melt partitioning of He, Ar, and CO_2 for Ol and Cpx are as follows: ${}^{Ol/melt}D_{He} = 1.7 \times 10^{-4}$, ${}^{Ol/melt}D_{Ar} = 1.1 \times 10^{-3}$, ${}^{Ol/melt}D_{CO2} = 7 \times 10^{-4}$ (assumed in order to fit data), ${}^{Cpx/melt}D_{He} = 2 \times 10^{-4}$, and ${}^{Cpx/melt}D_{Ar} = 1.1 \times 10^{-3}$. The starting conditions for modeling are He $= 5 \times 10^{-11}$ mol/g, He/$Ar^* = 1.3$, and He/$CO_2 = 3.3 \times 10^{-5}$.

from at least one additional process postdating the partial melting. Matusiak-Małek et al. (2017) argued that xenoliths from WG reflect a polyphase lithospheric mantle evolution, which started with up to 30% of melting from the protolith that left a harzburgitic residuum, with this residuum subsequently metasomatized by carbonated hydrous silicate melt related to Cenozoic volcanism (see section Petrological Background). This metasomatic event is responsible for the recrystallization of Cpx, Opx (at least partially), and amphiboles, resulting in the entrapment of secondary FI (e.g., **Figure S5D**) whose chemical and isotope composition resemble that of fluids dissolved in the metasomatizing agent. Matusiak-Małek et al. (2017) highlighted that the enrichment of LREE in Cpx relative to primitive mantle is a proxy of a metasomatic process, and that both Cpx itself as well as Opx (at least partially) have to be considered secondarily. Such a metasomatic history is typical for the lithospheric mantle located beneath the northern margin of the Bohemian Massif (e.g., Brandl et al., 2015), although WG is the only locality where hydrous minerals have been found.

Considering that we measured progressively lower He/^{40}Ar*, He/^{21}Ne* (not shown), He/N_2^*, and He/CO_2 ratios in Opx and

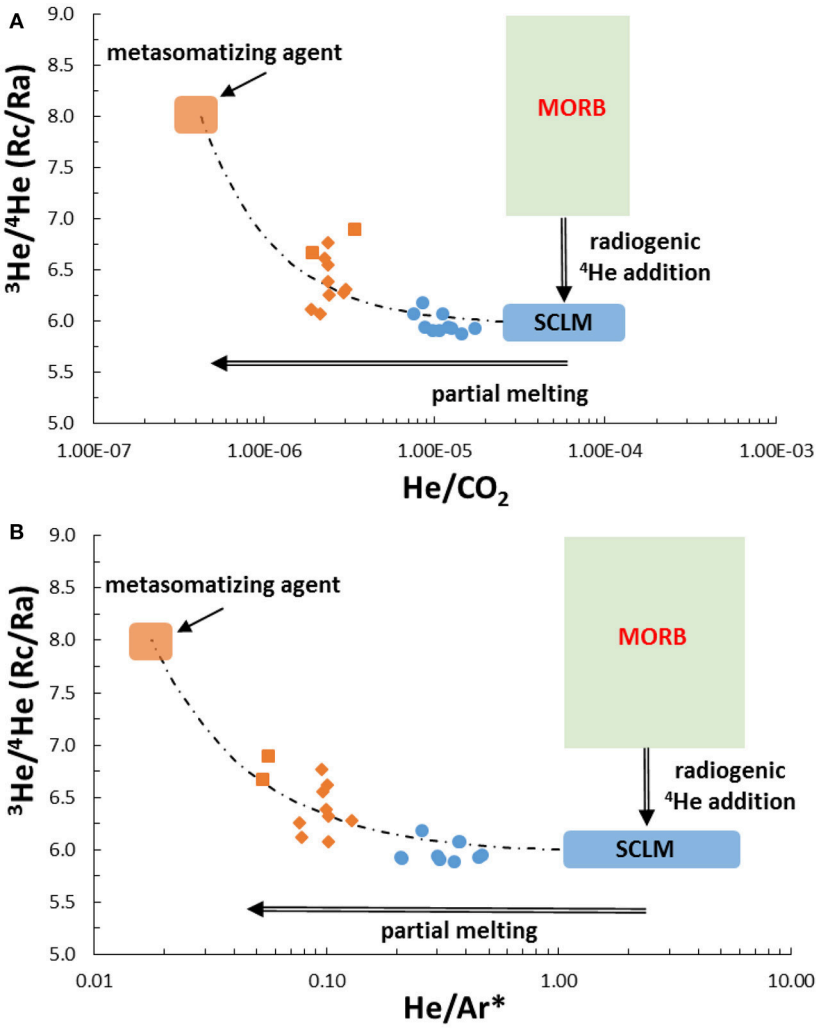

FIGURE 10 | He/CO_2 and He/Ar^* vs. $^3He/^4He$ corrected for air contamination (Rc/Ra values). The green, blue, and orange rectangles are the same as in **Figure 7**. The black dotted line represents binary mixing between two endmembers: (1) the residual mantle (blue rectangle) having $He/CO_2 = 2.5 \times 10^{-5}$, $He/Ar^* = 1$, and $^3He/^4He = 6$ Ra, and (2) the metasomatic agent (orange rectangle) having $He/CO_2 = 3.7 \times 10^{-7}$, $He/Ar^* = 1.7 \times 10^{-2}$, and $^3He/^4He = 8$ Ra. The symbols are the same as in **Figure 5**.

Cpx than in Ol (**Table 3** and **Figures 8**, **9**, **11** and **Figure S6**), it is reasonable to suppose that the fluids entrapped during metasomatism were somehow depleted in He and rich in CO_2. Cpx shows the highest $^3He/^4He$ ratios close to the lower limit of MORB (**Figure 6**), indicating that fluids associated with the metasomatic agent originally had a MORB-like signature. This can also be observed in the C-isotope composition of CO_2, although it is less evident, which manifests in Opx as a mean $\delta^{13}C$ of −4.1‰ (**Figure 7**), which is very close to the upper limit of the MORB range (−8‰ < $\delta^{13}C$ < −4‰; Marty and Jambon, 1987; Javoy and Pineau, 1991; Macpherson and Mattey, 1994; Sano and Marty, 1995; Deines, 2002). Unfortunately, it was not possible to make any measurement(s) in Cpx, which we would have expected to show values well within the MORB range. On the other hand, Ol has a mean $\delta^{13}C$ of −3.8‰ (**Figure 7**), which could indicate a slight contamination of the residual mantle—possibly due to limestone originating from an old subduction component—as also shown by the lowest $^3He/^4He$ ratio of our data set (∼6 Ra) (see section Inferences About the Mantle Features Beneath the North-Easternmost Part of the Eger (Ohře) Rift).

Considering that most of the studied Ol samples ($WG1_{II}$, $WG2_{II}$, $WG3_{II}$, $WG6_{II}$, $WG8_{II}$, and $WG9_{II}$) represent the residual mantle, while Cpx and some of the Opx (and Ol) samples ($WG4_{II}$, $WG7_{II}$, and $WG10_{II}$) are partially or completely modified by the metasomatic process, we argue that FI from Ol and Px represent a mixing of two endmembers: (1) a residuum after partial melting, characterized by narrow variability of $^3He/^4He$ (∼6 Ra) and $\delta^{13}C$ (∼ −3.8‰), and (2) a metasomatic agent, characterized by more-primitive and He-depleted fluids originating from an asthenosphere melt, originally with a

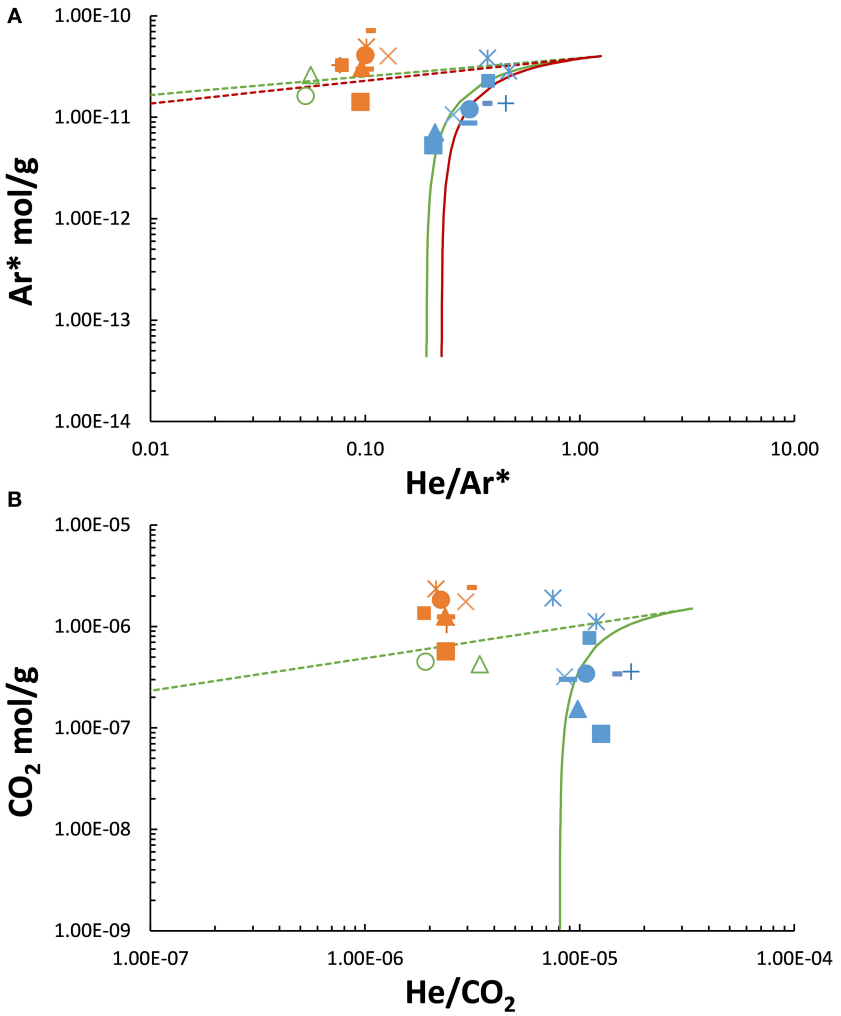

FIGURE 11 | (A) He/Ar* vs. Ar* concentration and **(B)** He/CO_2 vs. CO_2 concentration. The modeling of the modal batch and fractional equilibrium melting and starting conditions are the same as in **Figure 9**. The symbols are the same as in **Figure 9**.

MORB-like $^3He/^4He$ ratio (~8 Ra) and $\delta^{13}C$ ~ −4.2‰ (**Figures 7B**, **10**). This mixing hypothesis seems reasonable because our extraction procedure (single-step crushing) would result in the analysis of the total amount of FI released from crushing ~0.02 to ~1 g of crystals. We cannot exclude that these crystals contemporarily hosted primary and/or secondary FI (**Figures S5A–D**) belonging to the residual mantle and/or to the metasomatic agent. The boundary conditions of the mixing model were chosen as follows: for the residual mantle we assumed a mean $^3He/^4He$ ratio of 6 Ra, which is within the range of European SCLM (6.32 ± 0.39 Ra; Gautheron et al., 2005), while for the metasomatic agent we assumed the mean $^3He/^4He$ ratio of the MORB range (i.e., 8 Ra). Consequently, the He/CO_2 and $He/^{40}Ar^*$ ratios were chosen to fit our data. It should be noted that assuming lower $^3He/^4He$, He/CO_2, and $He/^{40}Ar^*$ ratios would not change the final interpretation, considering that the maximum $^3He/^4He$ ratio measured in Cpx is close to the lower limit of the MORB range (**Figure 10**).

Inferences About the Mantle Features Beneath the North-Easternmost Part of the Eger (Ohře) Rift

Origin of the $^3He/^4He$ Signature

The chemistry of FI coupled to the petrology of mantle xenoliths from WG provides evidence that a complex history of processes contributed to the local mantle composition at the time of the xenolith incorporation into the melts ascending in the volcanic system. The range of $^3He/^4He$ ratios measured in Ol and Px (5.9–6.9 Ra; **Figure 6**) suggests that the mantle beneath the north-easternmost part of the Eger (Ohře) Rift is slightly radiogenic relative to the typical MORB range (8 ± 1 Ra; e.g., Graham, 2002). This feature appears to be common to other central and western European magmatic provinces (i.e., Eifel, French Massif Central, Pannonian Basin, Calatrava, and Tallante; $^3He/^4He$ is 6.32 ± 0.39 Ra), whose noble gases in mantle xenoliths were analyzed using the same extraction method used in the present study (i.e., single-step crushing; Gautheron et al., 2005; Martelli

et al., 2011). Gautheron et al. (2005) discussed three interpretative models for justifying this signature in the SCLM: (1) the addition of ^{4}He-rich fluids/melts due to dehydration of the subducting plate (e.g., Yamamoto et al., 2004), (2) the recent and localized infiltration of a MORB-like He composition from the asthenosphere mixing with a more-radiogenic isotope signature residing in the lithosphere (e.g., Dunai and Porcelli, 2002), and (3) continuous (and extensive) He enrichment of SCLM in the steady state (see section Atmospheric Contamination; Gautheron and Moreira, 2002). All of these three models are valid, and they can explain the features of the mantle beneath the north-easternmost part of the Eger (Ohře) Rift and its closest surroundings.

We have already inferred a direct mantle contamination of atmospheric gases from dehydration of subducting oceanic crust (see section Atmospheric Contamination). This process could also account for contamination of a MORB-like source by radiogenic ^{4}He, finally resulting in residual mantle with a ^{3}He/^{4}He ratio of ∼6 Ra. In this respect, the model proposed by Faccenna et al. (2010) would perfectly fit this scenario. The second model is essentially the same as what we argue in Section Mantle Metasomatism occurring in the mantle beneath the study area. In this respect the residual mantle represented by Ol with Fo>89 could result from model 1 or be due to the steady-state conditions of SCLM established by the continuous metasomatic flux of MORB-like He from the asthenosphere and the production of radiogenic ^{4}He from the decay of U and Th in crustal rocks recycled into the mantle by previous subduction events (model 3). Instead, metasomatic fluids ascending from the asthenosphere are preferentially trapped in Cpx and have a MORB-like signature, as reflected in hypotheses 2 and 3.

Implications for the Source of Magmatism

The origin of CEVP magmatism is vigorously debated and far from being fully understood. Seismic tomography studies have inferred the presence of mantle plumes beneath certain regions, such as the French Massif Central and Eifel, whereas geochemical and petrological studies of erupted products seem to exclude this hypothesis (Lustrino and Carminati, 2007; Lustrino and Wilson, 2007). In alternative to classical plumes, a more recent and intriguing model proposed by Faccenna et al. (2010) invokes a subduction-triggered decompression melting. This debate might be resolvable by considering He and Ne isotopes, which represent powerful tracers for assessing the origin of fluids, although the latter are sensitive to air contamination. The proportion of primordial nuclides (^{3}He, and also ^{20}Ne and ^{22}Ne) is higher in the lower mantle than in the degassed MORB, which exhibits relatively uniform ratios (Ozima and Podosek, 1983; Moreira, 2013 and references therein). The plume-related magmatism is expected to have a ^{3}He/^{4}He ratio above the MORB range (>9 Ra) and a lower ^{21}Ne/^{22}Ne ratio for a given ^{20}Ne/^{22}Ne (i.e., a lower ratio of nucleogenic Ne to primordial Ne) than MORB melts (e.g., Moreira, 2013 and references therein). This has already been observed in classical hotspot settings such as the Galapagos Islands (**Figure 5**; Kurz et al., 2009) and Iceland, Reunion, and Hawaii (e.g., Rison and Craig, 1983; Kurz et al., 2009; Füri et al., 2010, 2011).

The ^{3}He/^{4}He ratios observed beneath the north-easternmost part of the Eger (Ohře) Rift (5.9–6.9 Ra) are significantly lower not only than typical plume-related ratios but also MORB-like ratios (**Figure 6**). As stated in Section 6.4.1, this range is comparable to those for other European regions where no plume is present (Gautheron et al., 2005; Moreira et al., 2018). However, while the above reasoning suggests that there is no compelling evidence of plume signatures beneath the study area, other studies have inferred a plume contribution in European mantle based on Ne and Xe isotopes, although the ^{3}He/^{4}He ratios are lower than expected for a mantle influenced by a plume (Buikin et al., 2005; Caracausi et al., 2016). We did not analyze Xe isotopes in the present study, instead we only evaluated Ne isotopes that showed that the FI included in the WG xenoliths are consistent with mixing between air and a MORB-like mantle (**Figure 5**). Our data also overlap the range of values found by Gautheron et al. (2005) when applying the same method (single-step crushing) to mantle xenoliths from the French Massif Central, Pannonian Basin, and Eifel, and those authors interpreted their results in the same way. Since Buikin et al. (2005) extracted FI from minerals using a less-conservative method (in terms of releasing noble gases from the crystal lattice), it is difficult to compare their results with ours. We therefore argue that the magmatism in the north-easternmost part of the Eger (Ohře) Rift probably does not originate from the presence of a mantle plume, and instead suggest alternative explanations such as lithosphere extension (Plomerová et al., 2007; Ulrych et al., 2011) or decompression melting (Faccenna et al., 2010).

Origin of CO_2

As indicated in previous sections, FI of mantle xenoliths from WG are dominated by CO_2, as observed in many other mantle xenoliths worldwide (Deines, 2002 and references therein; Gautheron et al., 2005; Sapienza et al., 2005; Correale et al., 2015; Créon et al., 2017). This finding was confirmed by Ladenberger et al. (2009) using Raman spectroscopy in a different suite of xenoliths from the same locality. Those authors reported that these mantle xenoliths contain large amounts of FI, and infer that their minimum entrapment depth is 31–38 km, which is consistent with both seismic evidence (Babuska and Plomerova, 2001; Majdanski et al., 2006) and petrological evidence (Matusiak-Małek et al., 2017 and references therein) from various xenoliths in the region. The presence of CO_2-rich inclusions represents evidence of fluid circulation within the local mantle (see section Mantle Metasomatism). Matusiak-Małek et al. (2017) argued that metasomatism involves the percolation of an alkaline silicate melt containing a CO_2-rich vapor phase rather than a true carbonatite, which is supported by the large amount of CO_2 released from FI and by δ^{13}C varying between −4.7‰ and −3.1‰ and not being related to the CO_2 concentration (**Figure 7A**). Such a lack of a correlation between δ^{13}C and the CO_2 concentration excludes any influence of magmatic degassing. In support of this, we modeled the trends in the variation of δ^{13}C, the CO_2 concentration, and the He/CO_2 ratio due to this process in the melt in both open- and closed-system equilibrium conditions (**Figures 7A,B**).

The boundary conditions used are reported in the caption of **Figure 7**.

The range of isotope ratios reported above is mostly close to the upper limit of the MORB range ($-8‰ < \delta^{13}C < -4‰$; Marty and Jambon, 1987; Javoy and Pineau, 1991; Macpherson and Mattey, 1994; Sano and Marty, 1995; Deines, 2002). However, allowing for the stated uncertainty (±0.3‰), the measured $\delta^{13}C$ values overlap those of primary igneous carbonatites ($-8‰ < \delta^{13}C < -5‰$; Jones et al., 2013 and references therein). In addition, the most-^{13}C-enriched values found in Ol ($\delta^{13}C$ up to −3.1‰) could indicate slight contamination of the residual mantle—possibly by recycled limestone—beneath the study area, as inferred by the $^3He/^4He$ ratio being the lowest for our data set (~6 Ra). This supports the recycling of sediments with a small proportion (<0.1%) of carbonate in the SCLM.

We also considered the relationship between $\delta^{13}C$ and the $CO_2/^3He$ ratio. **Figure 12** plots the FI data together with the ranges suggested for a MORB-like mantle ($-8‰ < \delta^{13}C < -4‰$ and $CO_2/^3He \sim 1–2 \times 10^9$; Sano and Marty, 1995) and limestone ($-1‰ < \delta^{13}C < +1‰$ and $CO_2/^3He \sim 1 \times 10^{13}$; Sano and Marty, 1995), as well as their relative mixing trends. As argued for the differences in the He/CO_2 ratio between Ol and Px (see sections Partial Melting of the Mantle and Mantle Metasomatism), we infer that the differences in the $CO_2/^3He$ ratio among mineral phases probably reflects mixing between a residual mantle characterized by $\delta^{13}C = -3.8‰$ and $CO_2/^3He \sim 3.6 \times 10^9$ and a metasomatic agent having $\delta^{13}C = -4.2‰$ (at the upper limit of MORB range) and $CO_2/^3He \sim 1.3 \times 10^{11}$. In detail, the geochemistry of FI in Px would result from the modification of residual mantle due to partial melting and metasomatism (see sections Partial Melting of the Mantle and Mantle Metasomatism). The residual mantle (i.e., SCLM) would represent a MORB-like mantle modified by the addition of <0.1% limestone presumably inherited by a previous (fossil) subduction event (**Figure 12**). It is worth noting that Correale et al. (2015) used a similar analytical approach to invoke a similar process for explaining the $\delta^{13}C$ signature of the mantle source beneath the Hyblean Plateau in southeast Sicily, Italy. Importantly, the average $\delta^{13}C$ values and $CO_2/^3He$ ratios of FI from Hyblean mantle xenoliths ($\delta^{13}C \sim -3.1‰$ and $CO_2/^3He \sim 5.1 \times 10^9$) fall within the ideal ranges assumed for the pure (unmetasomatized) residual mantle beneath the north-easternmost part of the Eger (Ohře) Rift (**Figure 12**). These data are actually consistent with the trend for binary mixing between a MORB mantle and limestone. Greater recycling into the mantle of carbonates, as occurs in certain active subduction settings (Aiuppa et al., 2017), would increase the proportion of limestone involved in this mixing. This has already been observed by Gennaro et al. (2017) in FI from cumulates from Stromboli arc volcano (Italy); those authors inferred that the local mantle wedge is contaminated by CO_2 coming from the decarbonation of the sediments carried by the subducting Ionian slab (**Figure 12**).

Comparison With Gases Emitted Along the Eger (Ohře) Rift

The Eger (Ohře) Rift is part of the ECRS and has been characterized by the occurrence of intense intraplate magmatism (e.g., Prodehl et al., 1995; Ulrych et al., 2011, 2016; Andreani et al., 2014). Although there is currently no ongoing volcanic activity at the ECRS, the presence of strong CO_2 degassing and

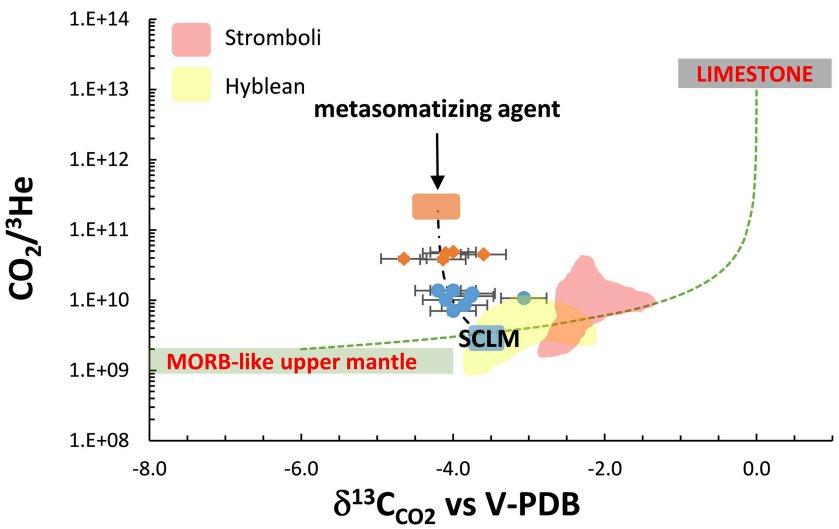

FIGURE 12 | C-isotope composition ($\delta^{13}C$) vs. $CO_2/^3He$. The green, blue, orange, and gray rectangles are the same as in **Figures 7**, **10**. Data from the Hyblean Plateau and Stromboli are from Correale et al. (2015) and Gennaro et al. (2017), respectively. The green dotted curve represents the binary mixing between a MORB-like upper mantle having $\delta^{13}C = -6‰$ and $CO_2/^3He = 2 \times 10^9$, and limestone having $\delta^{13}C = 0‰$ and $CO_2/^3He = 1 \times 10^{13}$ (Marty and Jambon, 1987; Javoy and Pineau, 1991; Sano and Marty, 1995). The black dotted line represents binary mixing between two endmembers: (1) the residual mantle (blue rectangle) having $CO_2/^3He = 4.8 \times 10^9$ and $\delta^{13}C = -3.5‰$, and (2) the metasomatic agent (orange rectangle) having $CO_2/^3He = 2.4 \times 10^{11}$ and $\delta^{13}C = -4‰$. The symbols are the same as in **Figure 5**.

persistent seismicity indicates that magmatism is still active at depth (Weinlich et al., 1999; Špaček et al., 2006; Hrubcová et al., 2017 and references therein). Most of the CO_2 degassing along the Eger (Ohře) Rift occurs in the central axis and shows a clear magmatic signature ($-4‰ < \delta^{13}C < -2‰$ and $^3He/^4He$ up to 6.3 Ra), while the magmatic component decreases with distance from the degassing locations, as indicated by decreasing $^3He/^4He$ ratios (Weinlich et al., 1999; Bräuer et al., 2004, 2008, 2011; Hrubcová et al., 2017 and references therein). As far as we are aware, the most-studied gas emissions are located in the western Eger (Ohře) Rift, at the boundary between Germany and the Czech Republic (i.e., Cheb Basin). The long-term monitoring of these emissions has revealed increasing $^3He/^4He$ ratios due to the link between ascending magmatic fluids and intracrustal seismicity (Bräuer et al., 2011). In contrast, the eastern Eger (Ohře) Rift has been subject to far less scrutiny, and to the best of our knowledge no He- and C-isotope data are available for surface gases. However, episodes of CO_2 emissions have been reported in the proximity of the main volcanic regions (e.g., Nízký Jeseník Mountains), and these might be related to the local magmatism (Špaček et al., 2006); however, this needs to be confirmed in a detailed study of the geochemistry of these fluids.

The lack of noble-gas measurements and CO_2-isotope data for gas emissions from the eastern Eger (Ohře) Rift makes it impossible to directly compare with our measurements in FI from WG mantle xenoliths. Nevertheless, considering that most of the magmatic gases emitted at or beneath the western Eger (Ohře) Rift (Bublák mofette, Cheb Basin) are interpreted as derived directly from the mantle beneath the region (Bräuer et al., 2004, 2008), we can make some comparative speculations. While the highest $^3He/^4He$ ratios measured for the Bublák mofette (up to 6.3 Ra; Bräuer et al., 2011) fall within the range of ratios measured in FI from WG (5.9–6.9 Ra), suggesting an homogeneous mantle source along the rift, $\delta^{13}C$ is significantly higher for the CO_2 emissions ($\delta^{13}C \sim -2‰$, Bräuer et al., 2008, 2011) than in FI ($-4.7‰ < \delta^{13}C < -3.1‰$). This discrepancy can be interpreted in two ways: (1) the mantle beneath the western Eger (Ohře) Rift has a slightly different isotope signature of CO_2, which is possibly related to interactions between carbonate-derived fluids and the residual mantle, or (2) $\delta^{13}C$ of mantle CO_2 is homogeneous along the Eger (Ohře) Rift, and the Bublák mofette emits gases that are slightly contaminated by intracrustal carbonate. The second hypothesis seems to be the most plausible given the homogeneous $^3He/^4He$ ratios along the Eger (Ohře) Rift and the presence of isolated carbonate deposits in the Cheb Basin (Buzek et al., 1996).

SUMMARY AND CONCLUSIONS

We have presented the first measurements of the concentration and isotope composition of noble gases and CO_2 in FI trapped in Ol and Px separated from ultramafic xenoliths hosted in WG basanite rocks that erupted a few tens of kilometers outside the north-easternmost part of the Eger (Ohře) Rift in Lower Silesia, southwest Poland. Data from FI were integrated with the evidence from petrography and geochemistry for minerals in order to define the mantle features beneath this sector of the European SCLM. This study highlights that Ol and Px (especially Cpx) may trap FI, recording different processes and timings that have occurred within the lithospheric mantle. The main results can be summarized as follows:

- Ultramafic xenoliths are mostly spinel-bearing harzburgites that sometimes contain amphiboles. Ol are classified into two groups based on forsterite contents: (1) $Fo_{88.9-91.5}$, which accounts for a fertile-to-residual mantle, and (2) $Fo_{85.5-88.1}$, which indicates large interactions with circulating (basic) melts. This dichotomy is also related to Opx and Cpx, which show two ranges of Mg# values (87–90 and 91–93, respectively) and clear evidence of recrystallization.
- The chemistry of FI is dominated by CO_2, with N_2 being the second-most-abundant species, and indicates that some Ol samples primarily represent a residual mantle depleted after various episodes of melt extractions, while the chemistry of Opx and Cpx suggests the overprinting of at least one metasomatic event postdating the partial melting. This event involved carbonated hydrous silicate melt related to Cenozoic volcanism that resulted in the entrapment of CO_2-rich inclusions. $\delta^{13}C$ relative to V-PDB is $-3.8\pm0.4‰$ in Ol and $-4.1\pm0.4‰$ in Opx, mostly falling at the upper limit of the MORB range ($-8‰ < \delta^{13}C < -4‰$), although a small percentage of carbonate recycling from a previous (fossil) subduction event cannot be excluded.
- The $^3He/^4He$ ratio corrected for air contamination (Rc/Ra values) is 6.7–6.9 Ra in Cpx, 6.3–6.8 Ra in Opx, and 5.9–6.2 Ra in Ol. The decrease in $^3He/^4He$ from Cpx to Ol is decoupled from the He concentration, thereby excluding any influence of diffusive fractionation from FI.
- The systematics of Ne and Ar isotopes indicate that most of the data are consistent with mixing between air and a MORB mantle. This evidence, together with that from the measured $^3He/^4He$ ratios, excludes the presence of a classical plume of the lower mantle beneath the study area. The geochemistry of FI results from a mixing of two endmembers: (1) the residual mantle, resulting from partial melting of European SCLM, and (2) the metasomatic agent, which is strongly He-depleted, CO_2-rich, and originally characterized by MORB-like $^3He/^4He$ ratios.

AUTHOR CONTRIBUTIONS

AR performed analyses of fluid inclusions, participated in mineral chemistry analyses, elaborated and interpreted data, conceptualized models, and drafted the manuscript and edited the final version. BP assisted in data elaboration and writing the final version of the manuscript. MC and CB collected samples. BP and GB prepared and interpreted thin sections, and handpicked minerals from mantle xenoliths. TN performed mineral chemistry analyses, and helped in petrography and mineral chemistry data interpretation. MC, TN, CB, MM-M,

and FI provided constructive comments on and edited the final version of the manuscript.

FUNDING

AR acknowledges financial support from Università degli Studi di Ferrara for the 2017 IUSS international mobility program during his PhD, as well as INGV-Palermo and the University of Vienna for providing analytical facilities.

ACKNOWLEDGMENTS

This work is part of the PhD (XXXII cycle) of ALR at the University of Ferrara. We thank Mariagrazia Misseri for helping in sample preparation, the isotope analysis of noble gases, and extracting CO_2 from fluid inclusions. We are grateful to Mariano Tantillo for his support in laboratory activities. We also thank Fausto Grassa, Giorgio Capasso, Ygor Oliveri, and Aldo Sollami for their efforts in the stable-isotopes laboratory. Michal Dajek is acknowledged for helping with map preparation. We thank the reviewers for useful suggestions that helped us to make the manuscript clearer and more complete. English language has been revised by English Science Editing (Paul Kolston).

SUPPLEMENTARY MATERIAL

The Supplementary Material for this article can be found online at: https://www.frontiersin.org/articles/10.3389/feart.2018.00215/full#supplementary-material

REFERENCES

Aiuppa, A., Fischer, T. P., Plank, T., Robidoux, P., and Di Napoli, R. (2017). Along-arc, inter-arc and arc-to-arc variations in volcanic gas CO_2/STratios reveal dual source of carbon in arc volcanism. *Earth-Science Rev.* 168, 24–47. doi: 10.1016/j.earscirev.2017.03.005

Allègre, J. C., Staudacher, T., and Sarda, P. (1987). Rare gas systematics: formation of the atmosphere, evolution and structure of the Earth's mantle. *Earth Planet. Sci. Lett.* 81, 127–150.

Andreani, L., Stanek, K. P., Gloaguen, R., Krentz, O., and Domínguez-González, L. (2014). DEM-based analysis of interactions between tectonics and landscapes in the Ore Mountains and Eger Rift (East Germany and NW Czech Republic). *Remote Sens.* 6, 7971–8001. doi: 10.3390/rs6097971

Babuska, V., and Plomerova, J. (2001). Subcrustal lithosphere around the Saxothuringian – Moldanubian Suture Zone – a model derived from anisotropy of seismic wave velocities. *Tectonophysics* 332, 185–199. doi: 10.1016/S0040-1951(00)00255-9

Barry, P. H., Hilton, D. R., Füri, E., Halldórsson, S. A., and Grönvold, K. (2014). Carbon isotope and abundance systematics of Icelandic geothermal gases, fluids and subglacial basalts with implications for mantle plume-related CO_2 fluxes. *Geochim. Cosmochim. Acta* 134, 74–99. doi: 10.1016/j.gca.2014.02.038

Battaglia, A., Bitetto, M., Aiuppa, A., Rizzo, A. L., Chigna, G., Watson, I. M., D'Aleo, R., Juárez Cacao, F. J., and de Moor, M. J. (2018). The Magmatic gas Signature of Pacaya Volcano, With Implications for the Volcanic CO_2 Flux From Guatemala. *Geochem. Geophys. Geosyst.* 19, 667–692. doi: 10.1002/2017GC007238

Białek, D., Raczyński, P., Sztajner, P., and Zawadzki, D. (2007). Archeocjaty wapieni wojcieszowskich. *Przegląd Geol.* 55, 1112–1116. Available online at: https://www.pgi.gov.pl/images/stories/przeglad/pg_2007_12_02_17.pdf

Birkenmajer, K., Pécskay, Z., Grabowski, J., and Lorenc,M. W., Zagożdżon, P. (2007). Radiometric dating of the Tertiary volcanics in Lower Silesia, Poland. V. K–Ar and palaeomagnetic data from late Oligocene to early Miocene basaltic rocks of theNorth-SudeticDepression. *Ann. Soc. Geol. Pol.* 77, 1–16.

Bonadiman, C., and Coltorti, M. (2011) Numerical modelling for peridotite phase melting trends in the SiO_2-Al_2O_3-FeO-MgO-CaO system at 2 GPa [abs.]. *Mineral. Magaz.* 75:548.

Brandl, P. A., Genske, F. S., Beier, C., Haase, K. M., Sprung, P., and Krumm, S. H. (2015). Magmatic evidence for carbonate metasomatism in the lithospheric mantle underneath the Ohře (Eger) Rift. *J. Petrol.* 56, 1743–1774. doi: 10.1093/petrology/egv052

Bräuer, K., Kämpf, H., Koch, U., and Strauch, G. (2011). Monthly monitoring of gas and isotope compositions in the free gas phase at degassing locations close to the Nový Kostel focal zone in the western Eger Rift, Czech Republic. *Chem. Geol.* 290, 163–176. doi: 10.1016/j.chemgeo.2011.09.012

Bräuer, K., Kämpf, H., Niedermann, S., Strauch, G., and Tesař, J. (2008). Natural laboratory NW Bohemia: comprehensive fluid studies between 1992 and 2005 used to trace geodynamic processes. *Geochem. Geophys. Geosyst.* 9, 1–30. doi: 10.1029/2007GC001921

Bräuer, K., Kämpf, H., Niedermann, S., Strauch, G., and Weise, S. M. (2004). Evidence for a nitrogen flux directly derived from the European subcontinental mantle in the Western Eger Rift, Central Europe. *Geochim. Cosmochim. Acta* 68, 4935–4947. doi: 10.1016/j.gca.2004.05.032

Buikin, A., Trieloff, M., Hopp, J., Althaus, T., Korochantseva, E., Schwarz, W. H., and Altherr, R. (2005). Noble gas isotopes suggest deep mantle plume source of late Cenozoic mafic alkaline volcanism in Europe. *Earth Planet. Sci. Lett.* 230, 143–162. doi: 10.1016/j.epsl.2004.11.001

Burnard, P. (2004). Diffusive fractionation of noble gases and helium isotopes during mantle melting. *Earth Planet. Sci. Lett.* 220, 287–295. doi: 10.1016/S0012-821X(04)00060-3

Burnard, P., Graham, D., and Turner, G. (1997). Vesicle-specific noble gas analyses of "popping rock": Implications for primordial noble gases in earth. *Science* 276, 568–571.

Burnard, P. G., Farley, K., a., and Turner, G. (1998). Multiple fluid pulses in a Samoan harzburgite. *Chem. Geol.* 147, 99–114. doi: 10.1016/S0009-2541(97)00175-7

Buzek, C., Holy, F., and Kvacek, Z. (1996). Early Miocene flora of the Cypris shale (Western Bohemia). *Acta Musei Nat. Prague B Hist. Naturalis* 52, 1–72.

Caracausi, A., Avice, G., Burnard, P. G., Füri, E., and Marty, B. (2016). Chondritic xenon in the Earth's mantle. *Nature* 533, 82–85. doi: 10.1038/nature17434

Coltorti, M., Downes, H., Grégoire, M., and O'Reilly, S. Y. (2009). Petrological evolution of the European Lithospheric Mantle: from Archean to present day. *J.Petrol.* 50:223. doi: 10.1093/petrology/egp046

Coltorti, M., Downes, H., Gregoire, M., and O'Reilly, S. Y. (2010). Petrological evolution of the European Lithospheric Mantle. *J. Geol. Soc. Lond.* 377:246. doi: 10.1144/SP337.1

Correale, A., Martelli, M., Paonita, A., Rizzo, A., Brusca, L., and Scribano, V. (2012). New evidence of mantle heterogeneity beneath the Hyblean Plateau (southeast Sicily, Italy) as inferred from noble gases and geochemistry of ultramafic xenoliths. *Lithos* 132–133, 70–81. doi: 10.1016/j.lithos.2011.11.007

Correale, A., Paonita, A., Rizzo, A., Grassa, F., and Martelli, M. (2015). The carbon-isotope signature of ultramafic xenoliths from the Hyblean Plateau (southeast Sicily, Italy): evidence of mantle heterogeneity. *Geochem. Geophys. Geosyst.* 16, 600–611. doi: 10.1002/2014GC005656

Correale, A., Rizzo, A. L., Barry, P. H., Lu, J., and Zheng, J. (2016). Refertilization of lithospheric mantle beneath the Yangtze craton in south-east China: evidence from noble gases geochemistry. *Gondwana Res.* 38, 289–303. doi: 10.1016/j.gr.2016.01.003

Créon, L., Rouchon, V., Youssef, S., Rosenberg, E., Delpech, G., Szabó, C., et al. (2017). Highly CO_2-supersaturated melts in the Pannonian lithospheric mantle – A transient carbon reservoir? *Lithos* 286–287, 519–533. doi: 10.1016/j.lithos.2016.12.009

Ćwiek, M., Matusiak-Małek, M., Puziewicz, J., Ntaflos, T. (2018) Lithospheric mantle beneath NE part of Bohemian Massif and its rekation to overlying crust:

new insights from Pilchowice xenolith suite, Sudetes, SW Poland. *Int. J. Earth Sci.* 107,1731–1753 doi: 10.1007/s00531-017-1568-4

Day, J. M. D., Barry, P. H., Hilton, D. R., Burgess, R., Pearson, D. G., and Taylor, L. A. (2015). The helium flux from the continents and ubiquity of low-^{3}He/^{4}He recycled crust and lithosphere. *Geochim. Cosmochim. Acta* 153, 116–133. doi: 10.1016/j.gca.2015.01.008

Deines, P. (2002). The carbon isotope geochemistry of mantle xenoliths. *Earth Sci. Rev.* 58, 247–278. doi: 10.1016/S0012-8252(02)00064-8

Dèzes, P., Schmid, S. M., and Ziegler, P. A. (2004). Evolution of the European Cenozoic Rift System: Interaction of the Alpine and Pyrenean orogens with their foreland lithosphere. *Tectonophysics* 389, 1–33. doi: 10.1016/j.tecto.2004.06.011

Di Piazza, A., Rizzo, A. L., Barberi, F., Carapezza, M. L., De Astis, G., Romano, C., and Sortino, F. (2015). Geochemistry of the mantle source and magma feeding system beneath Turrialba volcano, Costa Rica. *Lithos* 232, 319–335. doi: 10.1016/j.lithos.2015.07.012

Downes, H., Thirlwall, M. F., and Trayhorn, S. C. (2001). Miocene subduction-related magmatism in southern Sardinia : Sr ± Nd- and oxygen isotopic evidence for mantle source enrichment. *J. Volcanol. Geotherm. Res.* 106. doi: 10.1016/S0377-0273(00)00269-9

Dunai, T. J., and Baur, H. (1995). Helium, neon, and argon systematics of the European subcontinental mantle: Implications for its geochemical evolution. *Geochim. Cosmochim. Acta* 59, 2767–2783. doi: 10.1016/0016-7037(95)00172-V

Dunai, T. J., and Porcelli, D. (2002). Storage and transport of noble gases in the subcontinental lithosphere. *Rev. Mineral. Geochem.* 47, 371–409. doi: 10.2138/rmg.2002.47.10

Faccenna, C., Becker, T. W., Lallemand, S., Lagabrielle, Y., Funiciello, F., and Piromallo, C. (2010). Subduction-triggered magmatic pulses: a new class of plumes? *Earth Planet. Sci. Lett.* 299, 54–68. doi: 10.1016/j.epsl.2010.08.012

Füri, E., Hilton, D. R., Halldórsson, S. A., Barry, P. H., Hahm, D., Fischer, T. P., and Grönvold, K. (2010). Apparent decoupling of the He and Ne isotope systematics of the Icelandic mantle: the role of He depletion, melt mixing, degassing fractionation and air interaction. *Geochim. Cosmochim. Acta* 74, 3307–3332. doi: 10.1016/j.gca.2010.03.023

Füri, E., Hilton, D. R., Murton, B. J., Hémond, C., Dyment, J., and Day, J. M. D. (2011). Helium isotope variations between Réunion Island and the Central Indian Ridge (17°-21°S): New evidence for ridge-hot spot interaction. *J. Geophys. Res. Solid Earth* 116, 1–17. doi: 10.1029/2010JB007609

Gautheron, C., and Moreira, M. (2002). Helium signature of the subcontinental lithospheric mantle. *Earth Planet. Sci. Lett.* 199, 39–47. doi: 10.1016/S0012-821X(02)00563-0

Gautheron, C., Moreira, M., and Allègre, C. (2005). He, Ne and Ar composition of the European lithospheric mantle. *Chem. Geol.* 217, 97–112. doi: 10.1016/j.chemgeo.2004.12.009

Gennaro, M. E., Grassa, F., Martelli, M., Renzulli, A., and Rizzo, A. L. (2017). Carbon isotope composition of CO_2-rich inclusions in cumulate-forming mantle minerals from Stromboli volcano (Italy). *J. Volcanol. Geotherm. Res.* 346, 95–103. doi: 10.1016/j.jvolgeores.2017.04.001

Graham (2002). Noble gas isotope geochemistry of mid-ocean ridge and ocean island basalts: characterization of mantle source reservoirs. *Rev. Mineral. Geochem.* 47, 247–317. doi: 10.2138/rmg.2002.47.8

Guillot, B., and Sator, N. (2011). Carbon dioxide in silicate melts: A molecular dynamics simulation study. *Geochim. Cosmochim. Acta* 75, 1829–1857. doi: 10.1016/j.gca.2011.01.004

Gurenko, A. A., Hoernle, K. A., Hauff, F., Schmincke, H. U., Han, D., Miura, Y. N., and Kaneoka, I. (2006). Major, trace element and Nd-Sr-Pb-O-He-Ar isotope signatures of shield stage lavas from the central and western Canary Islands: insights into mantle and crustal processes. *Chem. Geol.* 233, 75–112. doi: 10.1016/j.chemgeo.2006.02.016

Harrison, D., Barry, T., and Turner, G. (2004). Possible diffusive fractionation of helium isotopes in olivine and clinopyroxene phenocrysts. *Eur. J. Mineral.* 16, 213–220. doi: 10.1127/0935-1221/2004/0016-0213

Heber, V. S., Brooker, R. A., Kelley, S. P., and Wood, B. J. (2007). Crystal-melt partitioning of noble gases (helium, neon, argon, krypton, and xenon) for olivine and clinopyroxene. *Geochim. Cosmochim. Acta* 71, 1041–1061. doi: 10.1016/j.gca.2006.11.010

Heber, V. S., Wieler, R., Baur, H., Olinger, C., Friedmann, A., Burnett, D. S. (2009) Noble gas composition of the solar wind as collected by the Genesis mission. *Geochim. Cosmochim. Acta* 73, 7414–7432. doi: 10.1016/j.gca.2009.09.013

Hilton, D. R., Fischer, T. P., and Marty, B. (2002). Noble Gases and Volatile Recycling at Subduction Zones. *Rev. Mineral. Geochem.* 47, 319–370. doi: 10.2138/rmg.2002.47.9

Hilton, D. R., Hammerschmidt, K., Teufel, S., and Friedrichsen, H. (1993). Helium isotope characteristics of Andean geothermal fluids and lavas. *Earth Planet. Sci. Lett.* 120, 265–282. doi: 10.1016/0012-821X(93)90244-4

Hilton, D. R., McMurty, G. M., Kreulen, R. (1997). Evidence for extensive degassing of the Hawaiian mantle plume from helium-carbon relationship at Kilauea volcano. *Geophys. Res. Lett.* 24, 3065–3068. doi: 10.1029/97GL03046

Hoefs, J. (2015). *Stable Isotope Geochemistry*. Cham: Springer International Publishing AG. doi: 10.1007/978-3-319-19716-6

Hrubcová, P., Geissler, W. H., Bräuer, K., Vavryčuk, V., Tomek, Č., and Kämpf, H. (2017). Active Magmatic Underplating in Western Eger Rift, Central Europe. *Tectonics* 36, 2846–2862. doi: 10.1002/2017TC004710

Ionov, D. A., and Hofmann, A. W. (2007). Depth of formation of sub-continental off-craton peridotites. *Earth Planetary Sci. Lett.*261, 620–634. doi: 10.1016/j.epsl.2007.07.036

Jambon, A., Weber, H., Braun, O. (1986). Solubility of He, Ne, Ar, Kr and Xe in a basalt melt in the rauge 1250-1600°C. *Geochemical implicactions. Geochim. Cosmochim. Acta* 50, 401–408. doi: 10.1016/0016-7037(86)90193-6

Javoy, M., and Pineau, F. (1991). The volatiles record of a " popping " rock from the Mid-Atlantic Ridge at 14 ° N : chemical and isotopic composition of gas trapped in the *vesicles*. 107, 598–611. doi: 10.1016/0012-821X(91)90104-P

Jones, A. P., Genge, M., and Carmody, L. (2013). Carbonate melts and carbonatites. *Rev. Mineral. Geochem.* 75, 289–322. doi: 10.2138/rmg.2013.75.10

Kaneoka, I. (1983). Noble gas constraints on the layered structure of the mantle. *Nature* 302, 698–700. doi: 10.1038/302698a0

Kryza, R., Willner, A. P., Massonne, H. J., Muszyński, A., and Schertl, H. P. (2011). Blueschist-facies metamorphism in the Kaczawa Mountains (Sudetes, SW Poland) of the Central-European Variscides: P-T constraints from a jadeite-bearing metatrachyte. *Mineralog. Magaz.* 75, 241–263. doi: 10.1180/minmag.2011.075.1.241

Kurz, M. D., Curtice, J., Fornari, D., Geist, D., and Moreira, M. (2009). Primitive neon from the center of the Galápagos hotspot. *Earth Planet. Sci. Lett.* 286, 23–34. doi: 10.1016/j.epsl.2009.06.008

Kurz, M. K. (1986). Cosmogenic helium in a terrestrial igneous rock. *Nature* 320, 435–439. doi: 10.1038/320435a0

Ladenberger, A., Lazor, P., and Michalik, M. (2009). CO_2 fluid inclusions in mantle xenoliths from Lower Silesia (SW Poland): formation conditions and decompression history. *Eur. J. Mineral.* 21, 751–761. doi: 10.1127/0935-1221/2009/0021-1930

Leake, B., Woolley, A., Arps, C., Birch, W., Gilbert,M., Grice, J., et al. (1997). Nomenclature of amphiboles: report of the subcommittee on amphiboles of the International Mineralogical Association, Commission on New Minerals and Minerals Names. *Canad. Mineral.* (1997) 35, 219–246.

Lustrino, M., and Carminati, E. (2007). Phantom plumes in Europe and the circum-Mediterranean region. *Geol. Soc. Am. Spec. Pap.* 430, 723–745. doi: 10.1130/2007.2430(33)

Lustrino, M., and Wilson, M. (2007). The circum-Mediterranean anorogenic Cenozoic igneous province. *Earth-Science Rev.* 81, 1–65. doi: 10.1016/j.earscirev.2006.09.002

Macpherson, C., Mattey, D. (1994). Carbon isotope variations of CO_2 in Central Lau Basin basalats and ferrobasalts. *Earth Planet. Sci. Lett.* 121, 263–276. doi: 10.1016/0012-821X(94)90072-8

Majdanski, M., Grad, M., Guterch, A., SUDETES 2003 Working Group (2006). 2-D seismic tomographic and ray tracing modelling of the crustal structure across the Sudetes Mountains basing on SUDETES 2003 experiment data. *Tectonophysics* 413, 249–269. doi: 10.1016/j.tecto.2005.10.042

Martelli, M., Bianchini, G., Beccaluva, L., and Rizzo, A. (2011). Helium and argon isotopic compositions of mantle xenoliths from Tallante and Calatrava, Spain. *J. Volcanol. Geotherm. Res.* 200, 18–26. doi: 10.1016/j.jvolgeores.2010.11.015

Martelli, M., Rizzo, A. L., Renzulli, a., Ridolfi, F., Arienzo, I., and Rosciglione, a. (2014). Noble-gas signature of magmas from a heterogeneous mantle wedge: the case of Stromboli volcano (Aeolian Islands, Italy). *Chem. Geol.* 368, 39–53. doi: 10.1016/j.chemgeo.2014.01.003

Marty, B. (2012). The origins and concentrations of water, carbon, nitrogen and noble gases on Earth. *Earth Planet. Sci. Lett.* 313–314, 56–66. doi: 10.1016/j.epsl.2011.10.040

Marty, B., and Jambon, a. (1987). C3He in volatile fluxes from the solid Earth: implications for carbon geodynamics. *Earth Planet. Sci. Lett.* 83, 16–26. doi: 10.1016/0012-821X(87)90047-1

Matsumoto, T., Chen, Y., and Matsuda, J. (2001). Concomitant occurrence of primordial and recycled noble gases in the Earth's mantle. *Earth Planet. Sci. Lett.* 185, 35–47. doi: 10.1016/S0012-821X(00)00375-7

Matsumoto, T., Honda, M., McDougall, I., O'Really, S. Y., Norman, M., Yaxley, G. (2000). Noble gases in pyroxenites and metasomatised peridotites from the Newer Volcanics, southeastern Australia: implications for mantle metasomatism. *Chem. Geol.* 168, 49–73. doi: 10.1016/S0009-2541(00)00181-9

Matsumoto, T., Honda, M., McDougall, I., and O'Reilly, S. Y. (1998). Noble gases in anhydrous lherzolites from the Newer Volcanics, southeastern Australia: a MORB-like reservoir in the subcontinental mantle. *Geochim. Cosmochim. Acta* 62, 2521–2533.

Matsumoto, T., Pinti, D. L., Matsuda, J. I., and Umino, S. (2002). Recycled noble gas and nitrogen in the subcontinental lithospheric mantle: implications from N-He-Ar in fluid inclusions of SE Australian xenoliths. *Geochem. J.* 36, 209–217. doi: 10.2343/geochemj.36.209

Mattey, D. P. (1991). Carbon dioxide solubility and carbon isotope fractionation in basaltic melt. *Geochim. Cosmochim. Acta* 55, 3467–3473. doi: 10.1016/0016-7037(91)90508-3

Matusiak-Małek, M., Puziewicz, J., Ntaflos, T., GréGoire, M., Benoit, M., and KlüGel, A. (2014). Two contrasting lithologies in off-rift subcontinental lithospheric mantle beneath central Europec-the Krzeniów (SW Poland) case study. *J. Petrol.* 55, 1799–1828. doi: 10.1093/petrology/egu042

Matusiak-Małek, M., Puziewicz, J., Ntaflos, T., Grégoire, M., Kukuła, A., and Wojtulek, P. M. (2017). Origin and evolution of rare amphibole-bearing mantle peridotites from Wilcza Góra (SW Poland), Central Europe. *Lithos* 286–287, 302–323. doi: 10.1016/j.lithos.2017.06.017

Mazur, S., Aleksandrowski, P., Kryza, R., and Oberc-Dziedzic, T. (2006). The Variscan orogen in Poland. *Geol. Q.* 50, 89–118. Available online at: https://gq.pgi.gov.pl/article/view/7400/6050

Moreira, M. (2013). Noble gas constraints on the origin and evolution of earth's volatiles. *Geochem. Perspec.* 2, 229–230. doi: 10.7185/geochempersp.2.2

Moreira, M., Kunz, J., and Allegre, C. (1998). Rare gas systematics in popping rock: Isotopic and elemental compositions in the upper mantle. *Science (80-.).* 279, 1178–1181. doi: 10.1126/science.279.5354.1178

Moreira, M., Rouchon, V., Muller, E., and Noirez, S. (2018). The xenon isotopic signature of the mantle beneath Massif Central. *Geochemical Perspect. Lett.* 6, 28–32. doi: 10.7185/geochemlet.1805

Nuccio, P. M., Paonita, A., Rizzo, A., and Rosciglione, A. (2008). Elemental and isotope covariation of noble gases in mineral phases from Etnean volcanics erupted during 2001-2005, and genetic relation with peripheral gas discharges. *Earth Planet. Sci. Lett.* 272, 683–690. doi: 10.1016/j.epsl.2008.06.007

Ozima, M., Podosek, F. A. (1983). *Noble Gas Geochemistry*. New York, NY: Cambridge University Press.

Pécskay, Z., Birkenmajer, K. (2013). "Insight into the geochronology of Cenozoic alkaline basaltic volcanic activity in Lower Silesia (SW Poland) and adjacent areas," in *Basalt 2013 – Cenozoic Magmatism in Central Europe, Abstract and Excursion Guides*, eds J. Büchner, V. Rapprich, O. Tietz (Goerlitz: Czech Geological Survey; Prague and Seckneberg Museum of Natural History Görlitz), 66–67.

Plomerová, J., Achauer, U., Babuška, V., Vecsey, L., the BOHEMA working group (2007). Upper mantle beneath the Eger Rift (Central Europe): plume or asthenosphere upwelling? *Geophys. J. Int.* 169, 675–682. doi: 10.1111/j.1365-246X.2007.03361.x

Prodehl, C., Mueller, S., and Haak, V. (1995). "The European Cenozoic rift system," in *Continental rifts: Evolution, Structure, Tectonics. Developments in Geotectonics,* Vol. 25, eds K. H. Olsen (New York, NY: Elsevier). 133–212.

Rison, W., and Craig, H. (1983). Helium isotopes and mantle volatiles in Loihi Seamount and Hawaiian Island basalts and xenoliths. *Earth Planet. Sci. Lett.* 66, 407–426. doi: 10.1016/0012-821X(83)90155-3

Rizzo, A. L., Barberi, F., Carapezza, M. L., Di Piazza, A., Francalanci, L., Sortino, F., and D'Alessandro, W. (2015). New mafic magma refilling a quiescent volcano: evidence from He-Ne-Ar isotopes during the 2011-2012 unrest at Santorini, Greece. *Geochem. Geophys. Geosyst.* 16, 798–814. doi: 10.1002/2014GC005653

Robidoux, P., Aiuppa, A., Rotolo, S. G., Rizzo, A. L., Hauri, E. H., and Frezzotti, M. L. (2017). Volatile contents of mafic-to-intermediate magmas at San Cristóbal volcano in Nicaragua. *Lithos* 272–273. doi: 10.1016/j.lithos.2016.12.002

Roedder, E. (1984) Fluid inclusions reviews in mineralogy. *Mineral. Soc. Am.* 12, 644 doi: 10.1515/9781501508271

Sano, Y., Marty, B. (1995). Origin of carbon in fumarolic gas from island arcs. *Chem. Geol.* 119, 265–274. doi: 10.1016/0009-2541(94)00097-R

Sapienza, G., Hilton, D. R., and Scribano, V. (2005). Helium isotopes in peridotite mineral phases from Hyblean Plateau xenoliths (south-eastern Sicily, Italy). *Chem. Geol.* 219, 115–129. doi: 10.1016/j.chemgeo.2005.02.012

Sarda, P., Staudacher, T., and Allègre, C. J. (1988). Neon isotopes in submarine basalts. *Earth Planet. Sci. Lett.* 91, 73–88. doi: 10.1016/0012-821X(88)90152-5

Sawicki, L. (1995). *Geological Map of Lower Silesia With Adjacent Czech and German Territories (Without Quaternary Deposits)*. Warszawa: Polish Geological Institute.

Smulikowski, K., Kozłowska-Koch, M. (1984). Bazaltoidy Wilczej Góry koło Złotoryi (Dolny Śląsk) i ich enklawy. *Archiwum Mineralogiczne* 40, 53–104 (in Polish).

Špaček, P., Sýkorová, Z., Pazdírková, J., Švancara, J., and Havíř, J. (2006). Present-day seismicity of the south-eastern Elbe Fault System (NE Bohemian Massif). *Stud. Geophys. Geod.* 50, 233–258. doi: 10.1007/s11200-006-0014-z

Stuart, F. M., Lass-Evans, S., Fitton, J. G., and Ellam, R. M. (2003). High 3He/4He ratios in picritic basalts from Baffin Island and the role of a mixed reservoir in mantle plumes. *Nature* 424, 57–59. doi: 10.1038/nature01711

Trull, T. W., and Kurz, M. D. (1993). Experimental measurements of 3He and 4He mobility in olivine and clinopyroxene at magmatic temperatures. *Geochim. Cosmochim. Acta* 57, 1313–1324. doi: 10.1016/0016-7037(93)90068-8

Ulrych, J., Dostal, J., Adamović, J., Jelínek, E., Špaček, P., Hegner, E., et al. (2011). Recurrent Cenozoic volcanic activity in the Bohemian Massif (Czech Republic). *Lithos* 123, 133–144. doi: 10.1016/j.lithos.2010.12.008

Ulrych, J., Krmíček, L., Tomek, Č., Lloyd, F. E., Ladenberger, A., Ackerman, L., and Balogh, K. (2016). Petrogenesis of Miocene alkaline volcanic suites from western Bohemia: Whole rock geochemistry and Sr-Nd-Pb isotopic signatures. *Chemie der Erde Geochem.* 76, 77–93. doi: 10.1016/j.chemer.2015.11.003

Upton, B. G. J., Downes, H., Kirstein, L. A., Bonadiman, C., Hill, P. G., and Ntaflos, T. (2011) The lithospheric mantle and lower crust-mantle relationships under Scotland: a xenolithic perspective. *J. Geol. Soc.* 168, 873–886. doi: 10.1144/0016-76492009-172

Valbracht, P. J., Honda, M., Matsumoto, T., Mattielli, N., McDougall, I., Ragettli, R. et al. (1996). Helium, neon and argon isotope systematics in Kerguelen ultramafic xenoliths: implications for mantle source signatures. *Earth Planet. Sci. Lett.* 138, 29–38. doi: 10.1016/0012-821X(95)00226-3

Weinlich, F. H., Bräuer, K., Kämpf, H., Strauch, G., Tesař, J., and Weise, S. M. (1999). An active subcontinental mantle volatile system in the western Eger rift, Central Europe: Gas flux, isotopic (He, C, and N) and compositional fingerprints. *Geochim. Cosmochim. Acta* 63, 3653–3671. doi: 10.1016/S0016-7037(99)00187-8

Wilson, M., and Downes, H. (2006). Tertiary-Quaternary intra-plate magmatism and mantle dynamics in Europe. *Cent. Eur.* 32, 147–166. doi: 10.1144/GSL.MEM.2006.032.01.09

Yamamoto, J., Kaneoka, I., Nakai, S., Kagi, H., Prikhod'ko, V. S., and Arai, S. (2004). Evidence for subduction-related components in the subcontinental mantle from low 3He/4He and 40Ar/36Ar ratio in mantle xenoliths from Far Eastern Russia. *Chem. Geol.* 207, 237–259. doi: 10.1016/j.chemgeo.2004.03.007

Yamamoto, J., Nishimura, K., Sugimoto, T., Takemura, K., Takahata, N., and Sano, Y. (2009). Diffusive fractionation of noble gases in mantle with magma channels: origin of low He/Ar in mantle-derived rocks. *Earth Planet. Sci. Lett.* 280, 167–174. doi: 10.1016/j.epsl.2009.01.029

Conflict of Interest Statement: The authors declare that the research was conducted in the absence of any commercial or financial relationships that could be construed as a potential conflict of interest.